Three-dimensional obstacle avoidance and path planning for unmanned underwater vehicles using elastic bands

Herman Biørn Amundsen
Department of Engineering Cybernetics
Norwegian University of Science and Technology
Trondheim, Norway
herman.b.amundsen@ntnu.no

Martin Føre
Department of Engineering Cybernetics
Norwegian University of Science and Technology
Trondheim, Norway
martin.fore@ntnu.no

Sveinung Johan Ohrem
Department of Aquaculture Technology
SINTEF Ocean
Trondheim, Norway
sveinung.ohrem@sintef.no

Bent Oddvar Arnesen Haugaløkken
Department of Aquaculture Technology
SINTEF Ocean
Trondheim, Norway
bent.haugalokken@sintef.no

Eleni Kelasidi
Department of Aquaculture Technology
SINTEF Ocean
Trondheim, Norway
eleni.kelasidi@sintef.no

Abstract

Unmanned underwater vehicles (UUVs) have become indispensable tools for inspection, maintenance, and repair operations in the underwater domain. The major focus and novelty of this work is collision-free autonomous navigation of UUVs in dynamically changing environments. Path planning and obstacle avoidance are fundamental concepts for enabling autonomy for mobile robots. This remains a challenge, particularly for underwater vehicles operating in complex and dynamically changing environments. The elastic band method has been a suggested method for planning collision-free paths and is based on modeling the path as a dynamic system that will continuously be reshaped based on its surroundings. This paper proposes adaptations to the method for underwater applications and presents a thorough investigation of the method for 3D path planning and obstacle avoidance, both through simulations and extensive lab and field experiments. In the experiments, the method was used by a UUV operating autonomously at an industrial-scale fish farm and demonstrated that the method was able to successfully guide the vehicle through a challenging and constantly changing environment. The proposed work has broad applications for field deployment of marine robots in environments that require the vehicle to quickly react to changes in its surroundings.

1 Introduction

1.1 Background

Unmanned underwater vehicles (UUVs) play an important role in monitoring and interacting with the oceans, and are widely used for mapping, or inspection, maintenance, and repair (IMR) operations for industry and research within fields such as research, oil and gas, military, oceanography, archaeology and aquaculture (Petillot et al., 2019; Shukla and Karki, 2016; Yu et al., 2019; Schjølberg and Utne, 2015; Føre et al., 2018). The use of UUVs has also replaced divers in dangerous operations in shallow waters (Holen et al., 2018) and enabled exploration of previously inaccessible deeper waters (Kyo et al., 1995).

In general, UUVs can be placed in two categories; autonomous underwater vehicles (AUVs) that are untethered and operate autonomously, and remotely operated vehicles (ROVs) that are usually tethered with an umbilical to a support vessel and manually controlled by a pilot. However, there is an ongoing effort to develop new methods that can support remote or autonomous ROV operations (Petillot et al., 2019; Schjølberg and Utne, 2015). Such operations can greatly reduce operational costs and can increase the weather window in which operations can safely be conducted.

Underwater environments pose unique engineering and scientific challenges due to their harsh and unforgiving nature. Vehicles must operate in the presence of hydrodynamical forces from waves and ocean currents (Faltinsen, 1990), with low bandwidths for wireless transmission due to high signal attenuation (Diamant et al., 2017), and in the absence of terrestrial technologies such as global navigation satellite systems (GNSS) (Fossen, 2021). Despite these challenges, autonomous operations are crucial for a wide range of applications in the marine domain. To safely operate autonomously in a real-world environment, a UUV must have some sort of strategy to handle spatial constraints due to static or moving obstacles.

Tasks such as path planning and obstacle avoidance become increasingly challenging when the vehicle must operate in an environment that changes over time. UUV operations in aquaculture is an example of such a case, where the vehicle operates in close proximity to living fish, flexible structures such as net pens (Klebert et al., 2015), other vehicles, and numerous other obstacles (e.g., ropes, sensors, and underwater cameras (Kelasidi and Svendsen, 2022)). The dense population of fish renders this a highly cluttered and complex space. Furthermore, the position and geometry of the net pens are ever-changing due to waves and currents, rendering the spatial constraints of the environment unknown. It is also a safety-critical environment, as structural failures might lead to fish escape incidents, which can have drastic economic and environmental consequences (Føre and Thorvaldsen, 2021). This dynamic and changing environment requires that a UUV is able to replan its path quickly such that it avoids disturbing or harming the fish, or damaging the net pen or itself. The use of UUVs for IMR operations in aquaculture has grown rapidly over the last decades (Balchen, 1991; Schjølberg and Utne, 2015; Føre et al., 2018; Kelasidi and Svendsen, 2022), and are often used for inspections of the structural integrity of the facilities, net cleaning operations for biofouling management, and biomass monitoring. This has resulted in a corresponding increase in research aimed at autonomous UUV operations in this field(Amundsen et al., 2022; Kelasidi et al., 2022; Cardaillac et al., 2023).The investigation of path planning and obstacle avoidance for aquaculture is an important component of this development.

The problem of finding the shortest collision-free path in a 3D space is known to be NP-hard (Canny and Reif, 1987) and planning algorithms thus tend to become computationally expensive. To mitigate the computational complexity, path planning are often categorized into local planning algorithms that only consider limited information and short time horizons, and global algorithms that take more information into account (Raja and Pugazhenthi, 2012). Because the computational costs of local algorithms are small, they are often suitable for real-time systems but are prone to making suboptimal decisions or getting stuck into local minima. Global algorithms, on the other hand, can calculate a path closer to the global minimum but are often infeasible for real-time systems. Usually, planning alogrithms must both react to sudden changes in the environment and plan optimal maneuvers, which have led to the development of hybrid architectures

consisting of both local and global algorithms (Wang et al., 2020).

The long-term goal of our research is to enable safe and reliant autonomy for UUVs in dynamically changing and cluttered environments such as aquaculture net cages. In this work, we limit the scope to local path planning and reactive obstacle avoidance. Future work can combine our contributions here with subjects such as obstacle detection, mapping, and global path planning in a hybrid architecture. The literature review, therefore, focuses on local path planning and obstacle avoidance, with an emphasis on real-time capabilities, applications to underwater domains, and experimental investigations.

1.2 Previous work

One of the first applications where collision-free path planning was a subject of research was in the robot manipulator research community in the 1980s. An early method was presented in Hanafusa et al. (1981), where the desired path is projected in the null space of the obstacles. Another method developed in the 1980s is the now famous potential field method (Khatib, 1985), in which the target applies an attractive artificial potential field onto a moving robot, while obstacles apply repulsive potential fields. The robot is then guided toward the target by following the valleys of the resulting potential field. The method represented an efficient and easy-to-conceptualize algorithm which is still an inspiration for many other methods. However, Koren and Borenstein (1991) exemplified shortcomings of the method, which include stability issues in the presence of narrow passages or obstacles.

One method inspired by the potential field method is the elastic band method (Quinlan and Khatib, 1993). The motivation of the elastic band method is to conceptualize the desired path as a physical system imitating a stretched elastic band. Instead of obstacles applying a potential field to the robot, they are applying a potential field to the desired path which will repel the path from the obstacles. Similarly, artificial contracting forces that simulate the internal tension of the rubber band are applied to the desired path, optimizing the path by removing any "slack" in the path. The method thus incorporates both obstacle avoidance and optimality with respect to path length elegantly in its planning algorithm. Letting the path be inspired by a physical system has an intuitive appeal - as the behavior of objects in the real world is well understood, this can make the method easier to conceptualize. The elastic band method has been implemented for helicopters (Lee and Tsai, 2011), ground vehicles (Sattel and Brandt, 2008; Brandt and Sattel, 2005), and an aquaculture net crawling robot (Føre et al., 2021). In (Wang et al., 2020), the method was combined with a global rapidly-exploring rapid tree (RRT) method (LaValle, 1998) in a hybrid architecture.

Alternatives to potential field-based methods include methods that are derived from vehicle kinematics or dynamics. A popular method is the dynamic window approach (Fox et al., 1997), which considers the dynamics of the robot. The possible desired trajectories are restricted to a valid search space where all trajectories render the robot able to stop before collisions. The optimal velocity maximizing the obstacle clearance and velocity within the search space is then selected. Tusseyeva et al. (2013) formulated the dynamic window approach for 3D AUV path planning. Another popular method is the velocity obstacle method (Tychonievich et al., 1989; Fiorini and Shiller, 1998), where the forward projection of the velocity vectors of obstacles are defined as velocity obstacles. To avoid collisions, the algorithm selects a velocity vector outside of these velocity obstacles. The velocity obstacle approach is extended to the 3D space for unmanned aerial vehicles in (Jenie et al., 2016). A third type of method is the constant avoidance algorithm proposed by (Savkin and Wang, 2013). The constant avoidance algorithm uses a constant heading angle calculated through the vehicle kinematics and makes the vehicle avoid collisions, while also compensating for the obstacle velocity vectors. This method was experimentally demonstrated for 3D obstacle avoidance using the HUGIN AUV in (Wiig et al., 2020).

Other approaches include the task-priority inverse kinematics framework (Simetti and Casalino, 2016) and the set-based task framework (Moe et al., 2020), where different control objectives such as path following, obstacle avoidance and singularity avoidance are prioritized relative to their respective importance. A control function is then used to choose the higher-priority control objective at each timestep. There also exist

methods based on formal verification, such as control-barrier functions (Ames et al., 2019) and the concept of Hamilton-Jacobi (HJ) reachability (Bansal et al., 2017). For approaches based on control-barrier functions, which play a role similar to Lyapunov theory in the study of the stability of dynamical systems, the forward invariance of some set can be designed such that it renders operational tasks as a safe set. Demonstrated applications includes legged robots (Nguyen et al., 2016), quad-copters (Wang et al., 2017), and surface vehicles (Thyri and Breivik, 2022).

Furthermore, recent developments in computational powers have rendered online trajectory optimization possible (Schulman et al., 2014). Approaches include methods that incorporate handling of state uncertainty (Majumdar and Tedrake, 2017; Xanthidis et al., 2023) and methods that combine optimization with HJ reachability (Chen et al., 2021). Model predictive control (MPC) methods have also been successfully applied, for instance for autonomous surface vessels (ASVs) that have to avoid collisions while complying with the COLREG convention (IMO, 1972; Johansen et al., 2016; Tengesdal et al., 2023).

1.3 Contributions

While obstacle avoidance is a thoroughly researched topic, there have been few experimental investigations of 3D underwater obstacle avoidance algorithms in dynamically changing environments. In such environments, there is a need for quickly being able to alter the plan based on changes in the surroundings. When the environment and the vehicle are subject to fast dynamics, the path planner is required to re-plan very fast, a requirement that few methods are able to fulfill in the 3D space. Furthermore, many methods are designed based on the dynamics of the vehicle, and, as such, it can be challenging to transfer the method between different vehicles. This paper adapts the elastic band algorithm for underwater vehicles and experimentally investigates its ability to produce safe paths in real-time in dynamically changing environments.

The elastic band algorithm is appealing due to its intuitiveness, low computational load, ability to incorporate both obstacle avoidance and optimization, and natural formulation in the 3D space. Furthermore, it is independent of the vehicle dynamics, which makes it easy to transfer between vehicles with different configurations and dynamics. To adapt the method to underwater environments, we also propose changes to the algorithm to incorporate the spatial constraint of the environment, including potential fields from the sea surface and seafloor. The path planner was implemented in a generalized control framework together with a guidance law, a set of super-twisting sliding mode motion controllers, and an extended Kalman filter (EKF) for state estimation. In the paper, we will present the entire proposed control framework to give a complete example of how the path planner can be implemented in a physical system. The method is demonstrated through numerical simulations using a mathematical model of an ROV, controlled lab experiments using a lightweight ROV, and field trials at a fish farm using an industrial ROV. In addition to demonstrating the ability to produce safe paths in cluttered environments, this set of trials also show-cases the versatility of the approach across scales.

1.4 Paper outline

Section 2 presents a mathematical model of an ROV. The elastic band path planner is then presented in Section 3, while Section 4 presents the control framework. Section 5 presents results from a simulation study and the laboratory experiment. Results from field experiments are then presented in Section 6 and Section 7 discusses the results and future prospects. Finally, 8 concludes the paper.

2 Vehicle Model

For simulation and notation purposes, we will here present a general model for an ROV, similar to the UUV used in the experiments. We assume that the ROV is designed such that the roll and pitch angles are

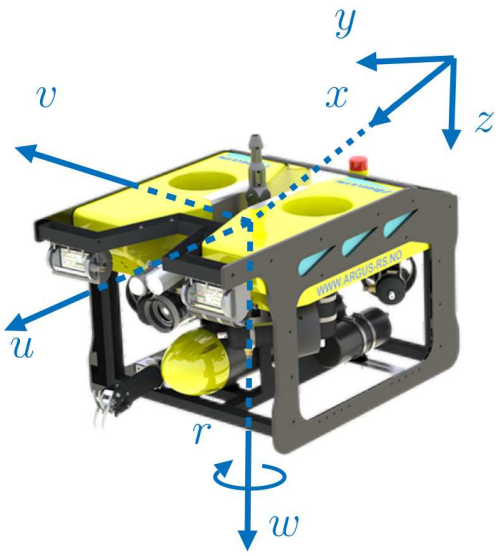

Figure 1: Illustration of the vehicle's position in the inertial frame (x, y, z) and velocity in the body-fixed frame (u, v, w, r). Image courtesy of Argus Remote Systems AS (Argus Remote Systems AS., 2023).

passively stabilized by gravity, and, therefore, we neglect these degrees of freedom (DOFs). Note that this is a common assumption for UUVs (Ohrem et al., 2022). The maneuvering model (Fossen, 2021, Ch. 6) of the vehicle is considered:

$$\begin{aligned} \dot{\boldsymbol{\eta}} &= \boldsymbol{J}(\psi)\boldsymbol{\nu} \\ \boldsymbol{M}\dot{\boldsymbol{\nu}} + \boldsymbol{C}(\boldsymbol{\nu})\boldsymbol{\nu} + \boldsymbol{D}(\boldsymbol{\nu})\boldsymbol{\nu} + \boldsymbol{g} &= \boldsymbol{\tau} + \boldsymbol{\tau}_{\text{wave}} + \boldsymbol{\tau}_{\text{current}} \, , \end{aligned} \tag{1}$$

where the generalized vector $\boldsymbol{\eta} \triangleq [\boldsymbol{p}^T, \psi]^T$ represents the position $\boldsymbol{p} = [x, y, z]^T$, and heading ψ of the vehicle in the inertial frame, and $\boldsymbol{\nu} \triangleq [\boldsymbol{v}^T, r]^T$ contains the linear velocity $\boldsymbol{v} = [u, v, w]^T$ and angular velocity r in the body frame (see Figure 1). The translation matrix

$$\boldsymbol{J}(\psi) = \begin{bmatrix} \boldsymbol{R}_z(\psi) & \boldsymbol{0}_{3x1} \\ \boldsymbol{0}_{1x3} & 1 \end{bmatrix} \tag{2}$$

relates the inertial frame and body frame, with $\boldsymbol{R}_z(\psi) \in SO(3)$ being the principal rotation matrix around the z-axis. The matrix $\boldsymbol{M} = \boldsymbol{M}^T > 0, \boldsymbol{M} \in \mathbb{R}^{4x4}$ is the system inertia matrix, $\boldsymbol{D}(\nu) \in \mathbb{R}^{4x4}$ is a damping matrix, the Coriolis and centripetal terms are contained in $\boldsymbol{C}(\boldsymbol{\nu}) \in \mathbb{R}^{4x4}$, while $\boldsymbol{g} = [0, 0, B - W, 0]^T$ is the vector of gravitational and buoyancy forces, with B and W referring to the vehicle buoyancy and weight, respectively. The environmental forces are contained in the vectors $\boldsymbol{\tau}_{\text{wave}}$ and $\boldsymbol{\tau}_{\text{current}}$, where $\boldsymbol{\tau}_{\text{wave}} \in \mathbb{R}^4$ contains the wave forces and $\boldsymbol{\tau}_{\text{current}} \in \mathbb{R}^4$ contains the generated force contribution from the ocean current in the body frame, both assumed to be bounded. As we will later estimate and control the absolute velocity of the vehicle, we choose to model the current forces as an unknown independent force rather than incorporating the current forces directly into the dynamics by utilizing the relative velocity between the vehicle and the water flow (Antonelli, 2018, Ch. 2.8.3). We make no assumptions about the irrotationality of the ocean currents, which can generally not be assumed to hold in aquaculture (Gansel et al., 2014). Finally, the vehicle is assumed to be actuated in 4 DOFs and $\boldsymbol{\tau} = \boldsymbol{B}\boldsymbol{f}$ note the generalized control forces. The thruster allocation matrix $\boldsymbol{B} \in \mathbb{R}^{4\times m}$ will distribute the generalized control forces $\boldsymbol{\tau} \in \mathbb{R}^4$ to the thruster input $\boldsymbol{f} \in \mathbb{R}^m$, where m is the number of thrusters, and will in general depend on the arrangement of thruster on the vehicle (Johansen and Fossen, 2013).

3 Elastic band path planner

The elastic band algorithm calculates a path from the vehicle position to a set of waypoints that is continuously reshaped by taking into account spatial constraints and the positions of obstacles. The vehicle control system can then use the path to steer the vehicle to the waypoints. This section outlines the elastic band planner by first describing the objective of the method and how the elastic band is built and structured. This is followed by descriptions of how artificial forces are used as proxies to describe internal tensions within the elastic band, the impacts of external obstacles and constraints, and how these contribute to deforming the elastic band structure.

3.1 Objective

The path planner's objective is to produce and update a collision-free path from one position to a set of waypoints. To target real-time performance, we simplify by letting the path planner overestimate the spaces occupied by the vehicle and obstacles to spheres and put no requirements on the vehicle orientation along the path. Note that since the vehicle is actuated in surge, sway, and heave, it can follow paths even without fixed requirements on its orientation. We can then let the configuration space and waypoints be defined in three DOFs. The set of k waypoints is denoted by $WP = \{\boldsymbol{w}_1, \boldsymbol{w}_2, \ldots, \boldsymbol{w}_k\}, \boldsymbol{w}_i \in \mathbb{R}^3$, while the configuration space is given by

$$\mathcal{C}_{\text{space}} = \{\boldsymbol{p} \in \mathbb{R}^3 \,|\, 0 \leq z \leq z_{\max}(x, y)\} \,, \tag{3}$$

where the depth is bounded between the surface and a max depth $z_{\max}(x, y) > 0$ (e.g., the depth of the seafloor at horizontal position x, y). Furthermore, let the obstacle space $\mathcal{C}_{\text{obs}}$ (i.e., the subset of $\mathcal{C}_{\text{space}}$ which is covered by obstacles) be defined as

$$\mathcal{C}_{\text{obs}} \triangleq \{\boldsymbol{p} \in \mathcal{C}_{\text{space}}, \mathcal{V}(\boldsymbol{p}) \cap \mathcal{O} \neq \emptyset\} \,, \tag{4}$$

where $\mathcal{V}(\boldsymbol{p}) \in \mathbb{R}^3$ is the volume covered by the vehicle and $\mathcal{O} \in \mathbb{R}^3$ the obstacle region. The free-space, $\mathcal{C}_{\text{free}}$, is then defined as the complement of $\mathcal{C}_{\text{obs}}$: $\mathcal{C}_{\text{free}} \triangleq \mathcal{C}_{\text{space}} \backslash \mathcal{C}_{\text{obs}}$. $\mathcal{C}_{\text{free}}$ is thus the part of $\mathcal{C}_{\text{space}}$ that is not covered by obstacles, and thus the area in which the vehicle can safely travel without colliding.

The objective is then to produce and update a continuous function $h : [0, 1] \times [\![0, k-1]\!] \to \mathcal{X}$, where $\mathcal{X}$ is a connected topological space (LaValle, 2006), such that $\forall s \in [0, 1]$ and $\forall i \in [\![0, k-1]\!]$,

$$h(s, i) = c_i(s) \tag{5}$$

$$c_i : [0, 1] \to \mathcal{C}_{\text{free}} \tag{6}$$

$$c_i(0) = \begin{cases} \boldsymbol{p}, & i = 0 \\ \boldsymbol{w}_i, & \text{else} \end{cases} \tag{7}$$

$$c_i(1) = \boldsymbol{w}_{i+1} \,, \tag{8}$$

or in simpler terms, h is a set of connected, collision-free paths from the vehicle that reaches all remaining waypoints.

We also make the simplifying assumptions that the waypoints are always feasible to reach (e.g., that they are never covered by obstacles), there always exists at least one connected path from the vehicle to all remaining waypoints, the obstacles do not move in an antagonist manner (i.e., they do not alter their trajectories to maximize the potential of a collision), and that obstacles do not move faster than the maximum speed of the vehicle. When evaluating the spatial constraints imposed by the sea surface, we disregard wave elevations and tidal shifts and assume that the sea surface is stationary at $z = 0$. We note that for sea operations of long durations, this assumption will no longer hold, and the spatial constraint will have to change with tidal shifts. However, for operations of short durations, similar to the cases investigated in this paper, this change can be neglected.

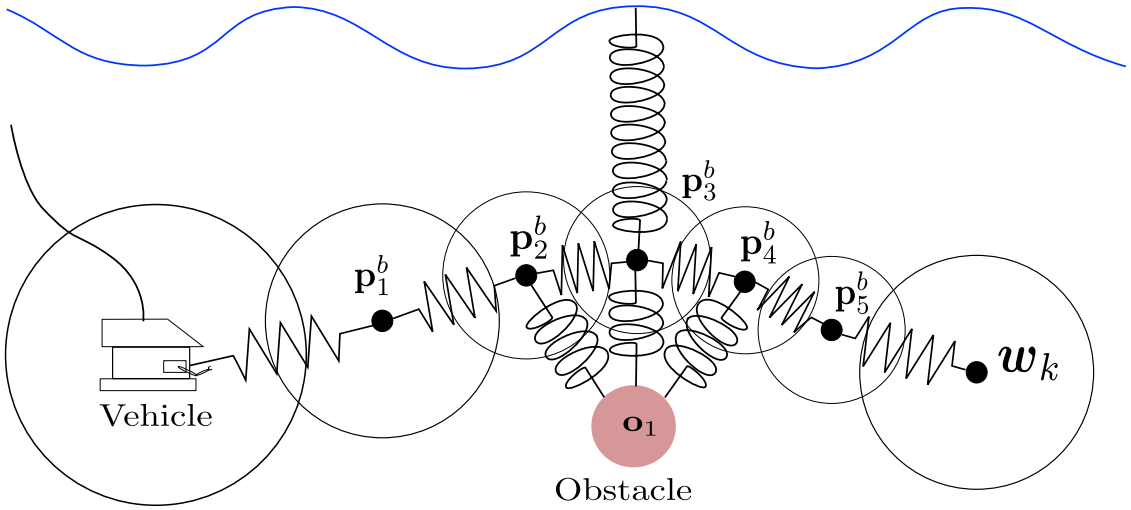

Figure 2: The discretized desired path is modeled as an elastic band where neighboring nodes apply retracting forces to the path, while obstacles and the sea surface apply repulsive forces.

3.2 The elastic band

The motivation behind the elastic band theory is to treat the desired path as a physical object, and as such give it dynamics inspired by a physical system, namely that of a stretched elastic material (Quinlan, 1994). This path, the elastic band, will then be subject to an internal energy potential that works to contract the band and external energy potentials that repel the band from obstacles and constraints. The former will thus optimize the path length, while the latter will enforce obstacle avoidance. These energy potentials will dynamically reshape the state of the elastic band such that the path is updated according to the environment at every time step.

We let the connected path h be approximated by a finite set C of discrete nodes. To ensure that the vehicle stays within $\mathcal{C}_{\text{free}}$ if moving along the path, each node is covered by a sphere $\boldsymbol{b}_i = [\boldsymbol{p}_i^{b^T} r_i^b]^T$ referred to as a bubble with position $\boldsymbol{p}_i^b = [x_i^b, y_i^b, z_i^b]^T$ centered on the node and radius $r_i^b > 0$. Furthermore, each bubble is a subset of $\mathcal{C}_{\text{free}}$, has a minimum radius, and an overlap $d_{\text{ol}} > 0$ with neighboring bubbles such that if the vehicle travels in a straight line between two consecutive bubbles, it stays entirely within the area covered by the bubbles and thus within $\mathcal{C}_{\text{free}}$. Figure 2 illustrates the concept of the desired path modeled as an elastic band.

3.3 Artificial forces

Since the elastic band is modeled as a dynamic system, its shape is manipulated by applying artificial forces. Internally, consecutive bubbles will apply contracting forces on each other. Let each bubble be connected to its neighbors with virtual linear springs according to Hooke's law, such that the i-th bubble will be subject to a quadratic internal potential energy, V_{int}, expressed as

$$\begin{aligned} V_{\text{int}}^i(\boldsymbol{p}_{i-1}^b, \boldsymbol{p}_i^b, \boldsymbol{p}_{i+1}^b) = &\frac{k_{\text{int}}}{2}\left(||\boldsymbol{p}_{i+1}^b - \boldsymbol{p}_i^b|| - r_{\min}\right)^2 \\ &+ \frac{k_{\text{int}}}{2}\left(||\boldsymbol{p}_i^b - \boldsymbol{p}_{i-1}^b|| - r_{\min}\right)^2, \end{aligned} \tag{9}$$

where $k_{\text{int}} > 0$ denotes the spring stiffness, $r_{\min}$ mimics the natural spring length, and $||\cdot||$ denotes the L^2 norm. The internal forces on bubble i can then be calculated from the gradient

$$\begin{aligned}\boldsymbol{f}^i_{\text{int}}(\boldsymbol{p}^b_{i-1}, \boldsymbol{p}^b_i, \boldsymbol{p}^b_{i+1}) =& -\nabla_{\boldsymbol{p}^b_i} V^i_{\text{int}}(\boldsymbol{p}^b_{i-1}, \boldsymbol{p}^b_i, \boldsymbol{p}^b_{i+1}) \\ =& k_{\text{int}} \frac{\boldsymbol{p}^b_{i+1} - \boldsymbol{p}^b_i}{||\boldsymbol{p}^b_{i+1} - \boldsymbol{p}^b_i||} \left(||\boldsymbol{p}^b_{i+1} - \boldsymbol{p}^b_i|| - r_{\min}\right) \\ &+ k_{\text{int}} \frac{\boldsymbol{p}^b_{i-1} - \boldsymbol{p}^b_i}{||\boldsymbol{p}^b_{i-1} - \boldsymbol{p}^b_i||} \left(||\boldsymbol{p}^b_{i-1} - \boldsymbol{p}^b_i|| - r_{\min}\right).\end{aligned} \tag{10}$$

Obstacles are defined similarly to bubbles, $\boldsymbol{o}_j = [\boldsymbol{p}^{oT}_j, r^o_j]^T$ with position $\boldsymbol{p}^o_j \in \mathbb{R}^3$ and radius $\boldsymbol{r}^o_j > 0$. They should apply repulsive forces on any nearby bubbles that decay exponentially with the distance between the obstacle and the bubble. Let the repulsive potential field from obstacle j to bubble i be modeled as

$$V^{i,j}_{\text{ext}}(\boldsymbol{b}_i, \boldsymbol{o}_j) = k_{\text{ext}} e^{-D_{\text{aff}}} \tag{11}$$

with

$$D_{\text{aff}} = ||\boldsymbol{p}^b_i - \boldsymbol{p}^o_j|| - r_{\min} - r^o_j - d_{\text{safe}}, \tag{12}$$

where $d_{\text{safe}} \geq 0$ is a safety margin set by the designer.

Equation (11) can be considered a nonlinear spring model with spring stiffness $k_{\text{ext}} > 0$ and no contracting component. Similarly to (10), the forces on $\boldsymbol{b}_i$ from $\boldsymbol{o}_j$ are given by the gradient

$$\begin{aligned}\boldsymbol{f}^{i,j}_{\text{ext}}(\boldsymbol{b}_i, \boldsymbol{o}_j) =& -\nabla_{\boldsymbol{p}^b_i} V^{i,j}_{\text{ext}}(\boldsymbol{p}^b_i, \boldsymbol{p}^o_j) \\ =& k_{\text{ext}} e^{-D_{\text{aff}}} \frac{\boldsymbol{p}^b_i - \boldsymbol{p}^o_j}{||\boldsymbol{p}^b_i - \boldsymbol{p}^o_j||}.\end{aligned} \tag{13}$$

To encapsulate the constraints from the sea surface and seafloor, we propose to add virtual potential fields from the surface and bottom of the sea. The potential from the sea surface on the i-th bubble is given by

$$V^i_{\text{surface}}(\boldsymbol{b}_i) = k_{\text{surface}} e^{-z^b_i}, \tag{14}$$

where $k_{\text{surface}} > 0$ is a designer parameter. The surface forces on bubble i are then given by the gradient

$$\begin{aligned}&\boldsymbol{f}^i_{\text{surface}}(\boldsymbol{b}_i) - \nabla_{\boldsymbol{p}^b_i} V^i_{\text{surface}} \\ &\quad = k_{\text{surface}} e^{-z^b_i} \frac{[0, 0, z^b_i]^T}{z^b_i}.\end{aligned} \tag{15}$$

Similarly, the potential field from the seafloor on bubble $\boldsymbol{b}_i$ is given by

$$V^i_{\text{seafloor}}(\boldsymbol{b}_i) = k_{\text{seafloor}} e^{-(z^b_i - z_{\max}(x^b_i, y^b_i) - r_{\min} - d_{\text{safe}})}, \tag{16}$$

with resulting forces

$$\begin{aligned}&\boldsymbol{f}^i_{\text{seafloor}}(\boldsymbol{b}_i) = -\nabla_{\boldsymbol{p}^b_i} V^i_{\text{seafloor}} \\ &= k_{\text{seafloor}} e^{-(z^b_i - z_{\max}(x^b_i, y^b_i) - r_{\min} - d_{\text{safe}})} \frac{[0, 0, z^b_i - z_{\max}(x^b_i, y^b_i)]^T}{z_{\max}(x^b_i, y^b_i) - z^b_i}.\end{aligned} \tag{17}$$

Here, $k_{\text{seafloor}} > 0$ is a design parameter.

Finally, the net forces onto bubble $\boldsymbol{b}_i$ from its neighboring bubbles and m obstacles are given by

$$\boldsymbol{f}^i_{\text{sum}} = \boldsymbol{f}^i_{\text{int}} + \boldsymbol{f}^i_{\text{surface}} + \boldsymbol{f}^i_{\text{seafloor}} + \sum_{j=0}^{m-1} \boldsymbol{f}^{i,j}_{\text{ext}}. \tag{18}$$

3.4 Reshaping of the elastic band

The new state of the elastic band can be found by calculating the state where each bubble has reached an equilibrium, i.e., when $\boldsymbol{f}^i_{\text{sum}} = 0$ for all i. This entails solving several highly nonlinear equations. However, a solution can be approximated by updating the position of each bubble by using a gradient descent method (Lemaréchal, 2012; Lee and Tsai, 2011).

To enforce that each bubble remains a subset of $\mathcal{C}_{\text{free}}$, bubble i is given the new radius

$$r_i^b = \begin{cases} r_{\max}, & \min\{||\boldsymbol{p}_i^b - \boldsymbol{p}_j^o|| - r_j^o, ||z_i^b - z_{\max}(x_i^b, y_i^b)||\} > r_{\max} \\ r_{\min}, & \min\{||\boldsymbol{p}_i^b - \boldsymbol{p}_j^o|| - r_j^o, ||z_i^b - z_{\max}(x_i^b, y_i^b)||\} < r_{\min} + d_{\text{safe}} \\ \min\{||\boldsymbol{p}_i^b - \boldsymbol{p}_j^o|| - r_j^o, ||z_i^b - z_{\max}(x_i^b, y_i^b)||\} - d_{\text{safe}}, & \text{otherwise,} \end{cases} \tag{19}$$

where $\boldsymbol{o}_j = [\boldsymbol{p}_j^o, r_j^o]^T$ represent the nearest obstacle and $r_{\max} > r_{\min}$ is an upper bound on the bubble radius.

Finally, the path is scanned for instances where either a bubble is redundant, i.e., when a bubble is completely covered by its neighbor, or if a bubble's neighbors overlap each other or if two neighboring bubbles no longer overlap, rendering the path disconnected. If a bubble is redundant, the following holds

$$|r_{i-1}^b - r_i^b| \geq ||\boldsymbol{p}_{i-1}^b - \boldsymbol{p}_i^b||, \tag{20}$$

or

$$r_{i-1}^b + r_{i+1}^b > ||\boldsymbol{p}_i^b - \boldsymbol{p}_{i-1}^b|| + ||\boldsymbol{p}_{i+1}^b - \boldsymbol{p}_i^b|| + d_{\text{ol}} \tag{21}$$

and the bubble is removed. Conversely, the path is rendered disconnected if

$$r_i^b + r_{i-1}^b - d_{\text{ol}} < ||\boldsymbol{p}_i^b - \boldsymbol{p}_{i-1}^b|| \tag{22}$$

and a bubble with suitable parameters is inserted. Finally, to ensure that the path stays collision-free and feasible, a new equilibrium state has to be re-calculated and evaluated after an insertion per Sections 3.3-3.4.

3.5 Algorithm

An implementation of the proposed method is described in the pseudo-code given in Algorithm 1. After first initializing a connected path, the artificial forces on bubbles (Sec. 3.3) and reshaping of the elastic band (Sec 3.4) are calculated in a loop until the final waypoint is reached. We also note that care should be taken when implementing (10), (13), (15), and (17) to avoid dividing by zero.

4 Control system

The control system is described using the guidance, navigation, and control (GNC) architecture (Fossen, 2021), as shown in Figure 3. The guidance system, consisting of the elastic band path planner and a guidance law, uses the positions of waypoints, obstacles, and the vehicle to calculate the reference signals for the control system. The low level control system then uses the reference signals and feedback of the vehicle states to calculate the control input for each thruster. Finally, the navigation system, consisting of an EKF, estimates the vehicle state based on sensor readings.

4.1 Guidance system

We utilize the elastic band path planner to calculate the desired path, where the positions of bubbles act as a set of intermediate waypoints. To transform the desired path into suitable reference signals for the motion controllers, we utilize a 3D guidance law. The guidance law will calculate a velocity vector pointing from the

Algorithm 1 The pseudo-code of the elastic band path planner

procedure ElasticBand
  Read a list of waypoints WP
  Initialize a connected path C from vehicle position to waypoints
  while $WP \neq \emptyset$ **do**
    Fetch current vehicle position $\boldsymbol{p}$ and obstacles $\mathcal{O} = [\boldsymbol{o}_0, \boldsymbol{o}_1, \cdots, \boldsymbol{o}_m]^T$
    Remove the first bubble $\boldsymbol{b}_o$ of C ▷ Shall rebase at $\boldsymbol{p}$
    while $||\boldsymbol{p} - \boldsymbol{p}_0^b|| \leq r_0^b$ **do**
      Remove $\boldsymbol{b}_o$ ▷ Remove additional reached bubbles and waypoints
    Insert a bubble at $\boldsymbol{p}$ to the start of C ▷ Path now starts at $\boldsymbol{p}$
    for $\boldsymbol{b}_i \in C, i > 0$ and $\boldsymbol{p}_i^b \notin WP$ **do**
      $\boldsymbol{f}_{\text{sum}}^i \leftarrow \boldsymbol{f}_{\text{int}}^i + \boldsymbol{f}_{\text{surface}}^i + \boldsymbol{f}_{\text{seafloor}}^i$ ▷ Eqs. (10), (15), (17)
      for $\boldsymbol{o}_j \in \mathcal{O}$ **do**
        $\boldsymbol{f}_{\text{sum}}^i \leftarrow \boldsymbol{f}_{\text{sum}}^i + \boldsymbol{f}_{\text{ext}}^{i,j}$ ▷ Eq. (13)
      $\boldsymbol{p}_i^b \leftarrow \text{argmin}||\boldsymbol{f}_{\text{sum}}^i||$
    for $\boldsymbol{b}_i \in C, i > 0$ and $\boldsymbol{p}_i^b \notin WP$ **do**
      Recalculate r_i^b ▷ Eq. (19)
      if $\boldsymbol{b}_i$ is redundant **then** ▷ Eqs. (20) or (21) holds true
        Remove $\boldsymbol{b}_i$
      if Path disconnected **then** ▷ Eq. (22) holds true
        Insert new bubble at $\frac{1}{2}(\boldsymbol{p}_i^b + \boldsymbol{p}_{i-1}^b)$
        Go back to 10

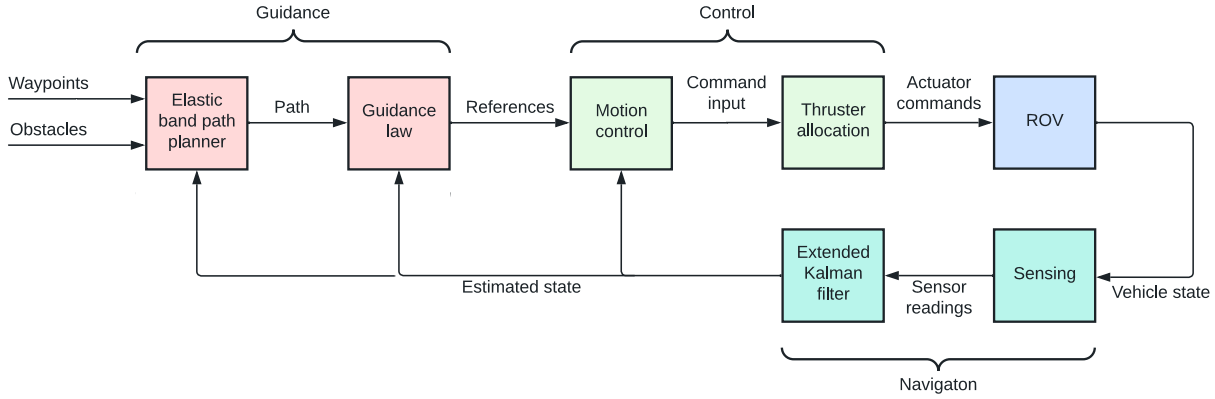

Figure 3: The block diagram of the guidance, navigation, and control system.

vehicle position $\boldsymbol{p}$ to the position of the next bubble $\boldsymbol{p}_1^b$ in the elastic band. Let the vector to the next bubble be $[\Delta x, \Delta y, \Delta z]^T = \boldsymbol{p}_1^b - \boldsymbol{p}$. The references for the velocity controllers are then given by (Breivik and Fossen, 2005)

$$\boldsymbol{v}_d = \begin{bmatrix} u_d \\ v_d \\ w_d \end{bmatrix} = \boldsymbol{R}_z(\psi)^T \boldsymbol{R}_z(\chi_d) \boldsymbol{R}_y(\Gamma_d) \begin{bmatrix} 1 \\ 0 \\ 0 \end{bmatrix} U_d(t), \tag{23}$$

where $\boldsymbol{R}_y(\cdot), \boldsymbol{R}_z(\cdot)$ are the principal rotation matrices about the y and z axes, respectively. Further,

$$\chi_d = \text{atan2}(\Delta y, \Delta x) \tag{24}$$

is the desired course angle,

$$\Gamma_d = \text{atan2}(-\Delta z, \sqrt{\Delta x^2 + \Delta y^2}) \tag{25}$$

is the desired elevation angle, and U_d is the desired speed.

As the radii of the bubbles in the elastic band will vary based on their clearances to obstacles, the bubble radii will thus reflect the complexity of the environment. We, therefore, choose to let the radius of the first bubble dictate the desired speed according to

$$U_d(t) = (r_0^b(t) - r_{\min}) \frac{U_{\max} - U_{\min}}{r_{\max} - r_{\min}} + U_{\min}, \tag{26}$$

where $U_{\max} \geq U_{\min} > 0$ represents the upper bound and lower bound to the desired speed, and $r_0^b(t)$ is the radius of the first bubble on the elastic band. Setting the desired speed to be proportional to the bubble radius will thus lead to a slower speed when in close proximity to obstacles and a faster speed when clear of obstacles. Furthermore, as r_0^b will decrease when nearing a waypoint, the desired speed will also decrease as the vehicle is approaching the waypoint, minimizing the chance that the vehicle will overshoot the waypoint. Finally, the reference for the heading controller is the desired course angle, i.e., $\psi_d = \chi_d$.

4.2 Low level control

To make the ROV follow the reference signals in velocity and heading, we employ the generalized super-twisting algorithm (GSTA) (Castillo et al., 2018; Haugaløkken et al., 2023). This is a higher-order sliding mode controller of order two. An advantage of second-order sliding mode compared to the more common order first-order sliding mode (Slotine and Li, 1991) is that it aims at making the control input continuous by placing the signum term in an augmented state which is then integrated. It is then able to attenuate chattering while maintaining the robust properties of sliding mode control (Castillo et al., 2018).

The sliding mode variable is defined as

$$\boldsymbol{\sigma} = \begin{bmatrix} \boldsymbol{v} - \boldsymbol{v}_d + \dot{\boldsymbol{v}} - \dot{\boldsymbol{v}}_d \\ \psi - \psi_d + 2(\dot{\psi} - \dot{\psi}_d) + \ddot{\psi} - \ddot{\psi}_d \end{bmatrix} \tag{27}$$

where $\dot{\boldsymbol{v}}_d, \dot{\psi}_d, \ddot{\psi}_d$ are calculated via appropriate reference models (Fossen, 2021, Ch. 12). We note that if $\boldsymbol{\sigma}$ converges to its origin, the origins of the tracking errors $\boldsymbol{v} - \boldsymbol{v}_d, \psi - \psi_d, \dot{\psi} - \dot{\psi}_d$ are globally exponentially stable equilibrium points.

The controller output is given by

$$\boldsymbol{\tau} = -\boldsymbol{K}_1 \boldsymbol{\phi}_1(\boldsymbol{\sigma}) + \boldsymbol{\sigma}_{\text{int}}, \tag{28}$$

where $\boldsymbol{\sigma}_{\text{int}}$ is the augmented state whose derivative is

$$\dot{\boldsymbol{\sigma}}_{\text{int}} = -\boldsymbol{K}_2 \boldsymbol{\phi}_2(\boldsymbol{\sigma}). \tag{29}$$

Furthermore,

$$\begin{aligned} \boldsymbol{\phi}_1(\boldsymbol{\sigma}) =& ||\boldsymbol{\sigma}||^{1/2} \text{sign}(\boldsymbol{\sigma}) + \boldsymbol{\beta}\boldsymbol{\sigma} \\ \boldsymbol{\phi}_2(\boldsymbol{\sigma}) =& ||\boldsymbol{\sigma}||^0 \text{sign}(\boldsymbol{\sigma}) + \frac{3}{2}||\boldsymbol{\sigma}||^{3/2} \text{sign}(\boldsymbol{\sigma}) + \boldsymbol{\beta}^2 \boldsymbol{\sigma}, \end{aligned} \tag{30}$$

where $\boldsymbol{K}_1, \boldsymbol{K}_2, \boldsymbol{\beta}$ are positive definite, diagonal matrices, and $\text{sign}(\cdot) \in \mathbb{R}^4$ is the vector equivalent of the signum function.

4.3 Navigation system

An EKF similar to the proposed observer in (Candeloro et al., 2012) is used as a state estimator. It considers a state space model

$$\begin{aligned} \dot{\boldsymbol{x}} &= \boldsymbol{F}(\boldsymbol{x}) + \boldsymbol{E}\boldsymbol{w} \\ \boldsymbol{y} &= \boldsymbol{H}\boldsymbol{x} + \bar{\boldsymbol{v}} \end{aligned}$$

with $\boldsymbol{x} \in \mathbb{R}^{12}$ being the state vector

$$\boldsymbol{x} = [\boldsymbol{\eta}^T, \boldsymbol{\nu}^T, \boldsymbol{b}^T]^T,$$

$\boldsymbol{y} \in \mathbb{R}^8$ the measurement vector, $\boldsymbol{w} \in \mathbb{R}^{12}$ and $\bar{\boldsymbol{v}} \in \mathbb{R}^8$ being zero-mean white-noise vectors, $\boldsymbol{E} \in \mathbb{R}^{12x12}$ is the process noise matrix, and $\boldsymbol{b} \in \mathbb{R}^4$ is a vector of bias terms used to model slowly varying forces. The state Jacobian is given by

$$\boldsymbol{F}(\boldsymbol{x}) = \begin{bmatrix} \boldsymbol{R}_z(\psi)\boldsymbol{\nu} \\ \hat{\boldsymbol{M}}^{-1} \begin{bmatrix} -\hat{\boldsymbol{D}}(\boldsymbol{\nu})\boldsymbol{\nu} & -\hat{\boldsymbol{C}}(\boldsymbol{\nu})\boldsymbol{\nu} \\ -\hat{\boldsymbol{g}}(\boldsymbol{\eta}) + \boldsymbol{R}_z^T(\psi)\boldsymbol{b} + \hat{\boldsymbol{\tau}} \end{bmatrix} \\ \boldsymbol{T}_b^{-1}\boldsymbol{b} \end{bmatrix},$$

where $\hat{\boldsymbol{M}}, \hat{\boldsymbol{D}}(\boldsymbol{\nu}), \hat{\boldsymbol{C}}(\boldsymbol{\nu}), \hat{\boldsymbol{g}}(\boldsymbol{\eta})$ are estimates of $\boldsymbol{M}, \boldsymbol{D}(\boldsymbol{\nu}), \boldsymbol{C}(\boldsymbol{\nu}), \boldsymbol{g}(\boldsymbol{\eta})$, the control input $\hat{\boldsymbol{\tau}}$ is an estimate of $\boldsymbol{\tau}$ calculated from the latest measured revolutions-per-minute (RPM) of the thrusters, and $\boldsymbol{T}_b$ is a positive definite design matrix. At each time-step, the Jacobian $\boldsymbol{F}(\boldsymbol{x})$ is linearized about the a posteriori state estimation $\hat{\boldsymbol{x}}_{k|k}$ before the system is discretized. The measurement matrix is given by $\boldsymbol{H} = [\text{diag}(\boldsymbol{1}_{8x1}), \boldsymbol{0}_{8x4}^T]^T$.

5 Simulations and lab trials

5.1 Simulations

In this section, simulation studies aimed at verifying and demonstrating the basic functionality of the elastic band method are presented. Examining the system in simulations prior to field tests has several advantages. First, it helps understand the challenges and limitations of the method prior to deployment. Secondly, we can quickly tune the design parameters without risking damage to the vehicle or the aquaculture facility. Finally, we are able to test the system in many different environmental conditions in a controlled setting.

5.1.1 Setup and configuration

The simulation environment was implemented in FhSim, a SINTEF Ocean developed modeling and simulation framework that offers a large collection of numerical models relevant for aquaculture and marine operations such as net pens, underwater vehicles, and fish behaviour (Reite et al., 2014; Su et al., 2019; Kelasidi et al., 2022). The simulations studies include two cases. In the first case study, an ROV is commanded to reach a set of four waypoints while simultaneously avoiding five dynamic obstacles. The second case study was set up with a virtual environment resembling that one might face at a fish farm, and was set up to mimic an operation where an ROV uses the elastic band planner to first plan a path to circumvent a net pen. A second vessel performing a docking operation next to the net pen then moves into the path of the ROV, acting as an obstacle and thus enforcing the adjustment of the path to avoid collision.

The simulation model of the ROV is presented in Appendix A. Model parameters and thruster allocation are based on the Argus Mini ROV, the same vehicle as used in the field experiments of this study, and the model

parameters were found using the WAMIT software (Lee, 1995). The net pen was simulated using the model presented in (Su et al., 2021) with a diameter of 50m, which is the standard size for the farming of Atlantic salmon, and can in generalized terms be described as a flexible cylinder with a conic shape bottom that will deform in response to water movements due to waves and currents. The obstacle vessel was simulated as a simple 3DOF surface vehicle with a length of $L_{oa} = 10$m and a beam of $B_{\max} = 4$m. The ocean current affecting the ROV, net pen, and obstacle vessel had a speed of 0.1m/s and a direction of 90°, while ocean waves were simulated using the JONSWAP spectrum (Fossen, 2021, Ch. 10.2) with a significant wave height of $H_s = 0.3$m, a mean wave period of $T_p = 4s$, and a direction of 90°.

To respect the spatial constraints from the moving net pen in the second case study, the elastic band path planner was set up to also consider repulsive forces from the net pen by adding forces acting onto bubble i from the net pen as found by:

$$\boldsymbol{f}_{\text{net}}^{i} = \begin{cases} k_{\text{net}} e^{-(||\boldsymbol{r}_{\text{net}}|| - r_{\min})} \frac{\boldsymbol{r}_{\text{net}}}{||\boldsymbol{r}_{\text{net}}||}, & \text{when } \boldsymbol{p}_i^b \text{ is outside of the net} \\ k_{\text{net}} e^{-\max(-1, (-||\boldsymbol{r}_{\text{net}}|| - r_{\min}))} \frac{\boldsymbol{r}_{\text{net}}}{||\boldsymbol{r}_{\text{net}}||}, & \text{when } \boldsymbol{p}_i^b \text{ is inside of the net} \end{cases} \tag{31}$$

where $k_{\text{net}} > 0$ is a design parameter, and $\boldsymbol{r}_{\text{net}}$ is the vector from the net panel closest to the bubble. The saturation in the exponential term was added to ensure that the exponential term does not grow large when a bubble is inside of the net pen, as this might lead to instability. The gains of the elastic band path planner were given according to $k_{\text{int}} = 10$, $k_{\text{ext}} = 10$, $k_{\text{net}} = 20$, $k_{\text{surface}} = 0.3$, $k_{\text{seafloor}} = 0$, while the minimum and maximum bubble radii were $r_{\min} = 0.9$ m and $r_{\max} = 5$ m, respectively. Desired overlap between adjacent bubbles was $d_{\text{ol}} = 0.65$ m, the safety margin was $d_{\text{safe}} = 0.3$ m, and the maximum and minimum desired speeds of the vehicle were $U_{\max} = 0.5$ m/s and $U_{\min} = 0.1$ m/s, respectively.

The motion controller in the simulation was the GSTA system presented in (28)-(30), and the gains were given by $\boldsymbol{K}_1 = \text{diag}(1, 1, 1, 2)$, $\boldsymbol{K}_2 = \text{diag}(5, 5, 10, 0.008)$, $\boldsymbol{\beta} = \text{diag}(10, 10, 15, 15)$. Unlike the field experiments where the vehicle states were estimated with sensors and an EKF, the simulations used the true vehicle states from the model as feedback to the control system.

5.1.2 Simulation results

The results from the first simulation case study can be seen in Figures 4-5. From the snapshots, it can be seen that the elastic band was successfully updated such that the bubbles stayed clear of the obstacles, and that the vehicle safely followed the desired path. The performance of the GSTA controller and the vehicle clearance to obstacles can be seen in Figure 5. Although the wave excitation force induced a high-frequent disturbance to the system, the motion controller was able to track its reference with good accuracy.

Figure 6 shows snapshots of the second simulation case study, where the ROV was commanded to travel from $\boldsymbol{p}_{\text{start}} = [-25, -30, 0]^T$ to $\boldsymbol{p}_{\text{goal}} = [5, 32, 6]^T$. Starting from position $\boldsymbol{p}_{\text{obs}} = [40, -30, 0]^T$, the obstacle vessel was commanded to dock next to the net pen at $\boldsymbol{p}_{\text{dock}} = [-25, 12, 0]^T$. From the figure, it can be seen how the net pen deforms, and how the obstacle vessel travels into the path of the ROV, thus requiring the elastic band path planner to update the path and vary the bubble size to avoid collisions. The performance of the GSTA controller can be seen in Figure 7, again demonstrating its ability to track its reference signals. Figure 7 also shows that the ROV avoided collisions during the simulation study. The simulation with 3D visualization, including the elastic band path planner, the net cage, the ROV, and the obstacle vessel, ran faster than real time with a step size of 0.033s (i.e., a frequency of 30 Hz), demonstrating the real-time capabilities of the elastic band algorithm.

5.2 Laboratory experiments

This section will present results from a preliminary laboratory experiment featuring the elastic band path planner. The laboratory experiments served as an early evaluation of the method and allowed us to identify challenges and improvements needed before final field deployment. The laboratory experiments utilized a

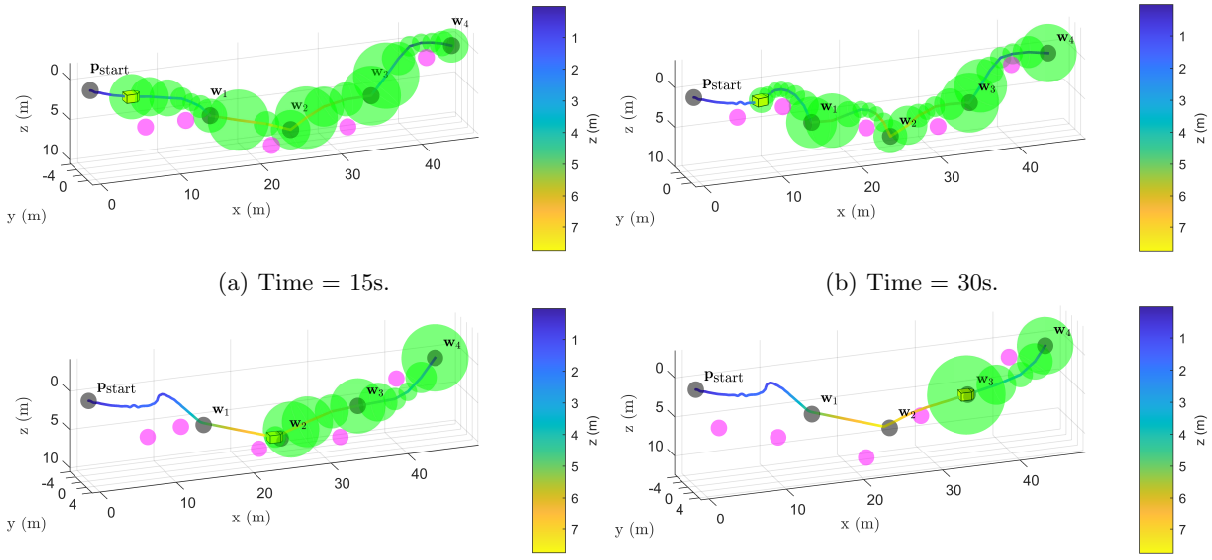

(a) Time = 15s.

(b) Time = 30s.

(c) Time = 100s.

(d) Time = 150s.

Figure 4: Snapshots from the first simulation study. The state of the elastic band can be seen in green, obstacles in magenta, waypoints in gray, and the ROV trajectory in colormap corresponding to the vehicle depth. Note that the apparent overlap between some bubbles and obstacles is only due to the 3D rendering, which does not fully show the deformation along the y-axis.

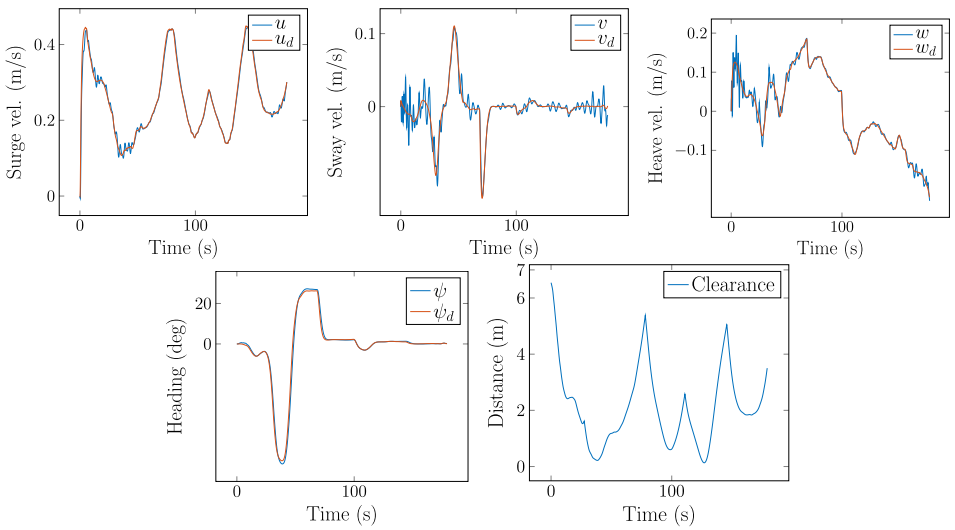

Figure 5: Reference tracking and obstacle clearance during the first simulation study.

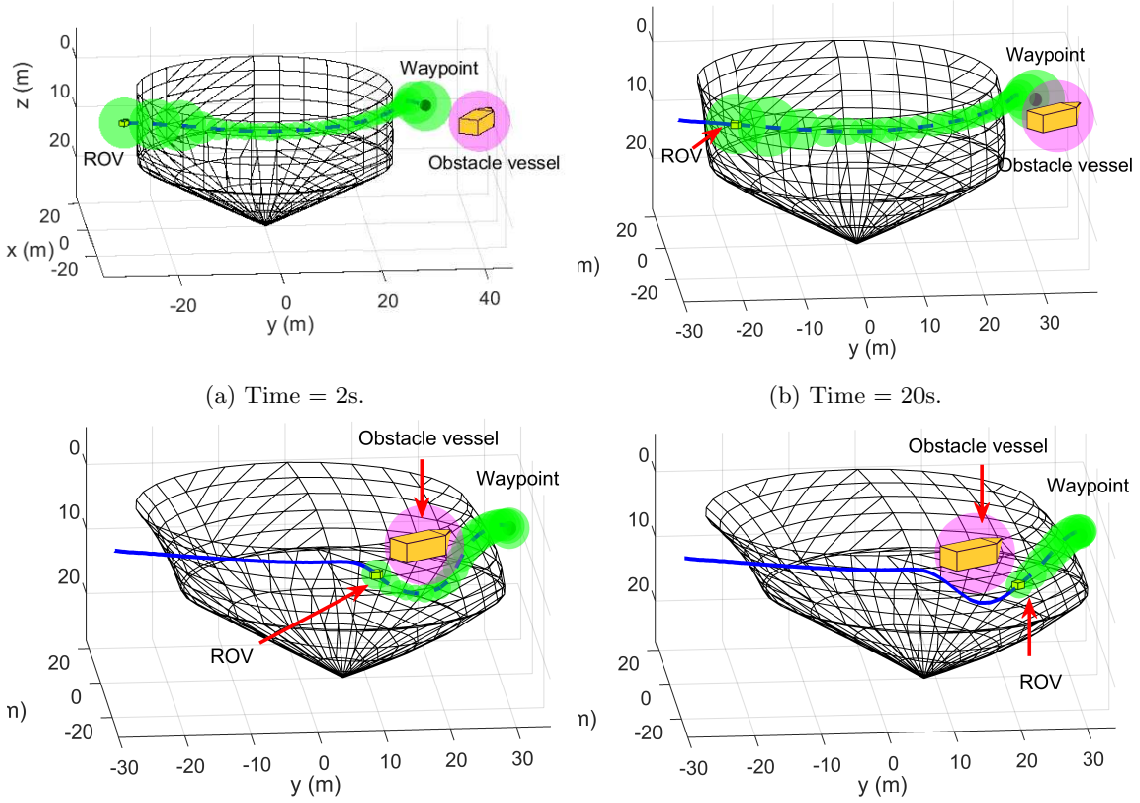

(a) Time = 2s.

(b) Time = 20s.

(c) Time = 120s.

(d) Time = 210s.

Figure 6: Snapshots from the second simulation study with ROV, net pen, and obstacle vessel. The state of the elastic band can be seen in green, while the trajectory of the ROV is marked in blue.

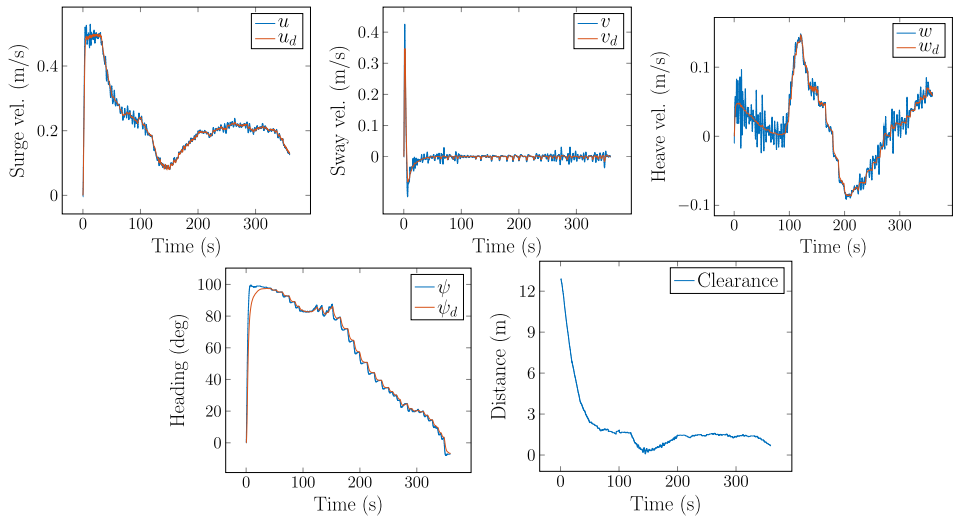

Figure 7: Reference tracking and obstacle clearance during the second simulation study.

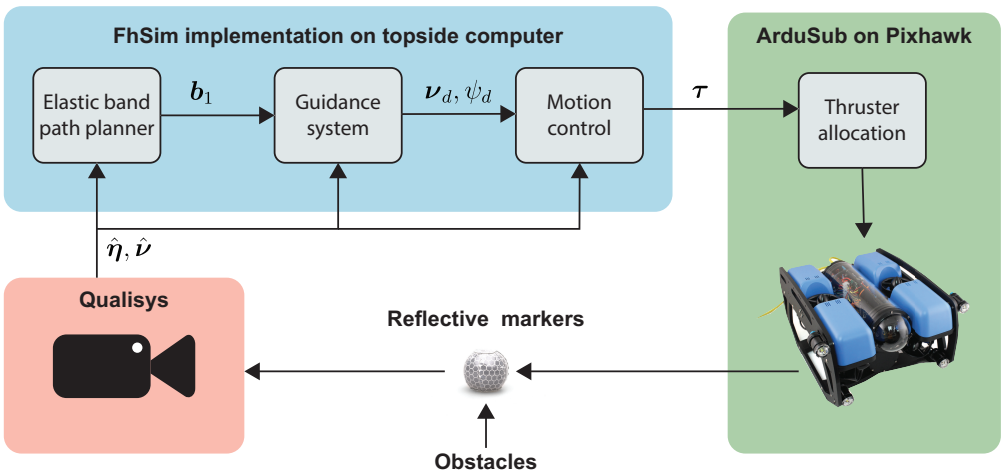

Figure 8: Block diagram of the control setup used in laboratory experiments.

different vehicle, which also serves to demonstrate the performance across different robotic platforms. Due to the early stage of the test and because of the different vehicle, the control system had some differences compared to the field deployment.

5.2.1 Setup and configuration

The experimental tests were conducted at the Marine Cybernetics Laboratory (MC-lab) at NTNU, Trondheim, which is a basin with dimensions $L \times W \times D = 40\text{m} \times 6.45\text{m} \times 1.5\text{m}$ (NTNU, 2022). The laboratory is fitted with six Oqus underwater cameras and the Qualisys motion tracking software (Qualisys AB, 2022), which together constitute a local positioning system. Light emitted by the system is reflected by markers that can be fixed to rigid bodies. The reflected light is then captured by the cameras, enabling the Qualisys software to estimate the position of the markers, and hence the position and orientation of the bodies they are attached to. The volume observed by the underwater cameras was $L \times W \times D = 12\text{m} \times 5.45\text{m} \times 1.35\text{m}$.

The vehicle used in the experiments was a BlueROV2 (Blue Robotics, Inc., 2022b), which is an observation class ROV with four horizontal and two vertical T200 thrusters arranged so that the ROV is actuated in surge, sway, heave, and yaw. The BlueROV2 weighs about 11 kg in air, is neutrally buoyant, and has dimensions $L \times W \times H = 0.457\text{m} \times 0.338\text{m} \times 0.254\text{m}$. The vehicle comes with the autopilot software ArduSub (Blue Robotics, Inc., 2022a) pre-installed on its onboard Pixhawk, and an on-board Raspberry Pi computer that relays communication between ArduSub and the topside computer. To enable Qualisys to estimate the position and orientation of the ROV, the vehicle was fitted with six markers. Moreover, a set of obstacles that were placed inside the basin were also fitted with markers such that Qualisys could detect their positions.

As these experiments used a different vehicle platform than the one used in the field trials in Section 6 and because of time constraints, the lab experiments were conducted using a simpler proportional-integral (PI) controller to control velocity and a first-order sliding mode controller (Antonelli, 2018) to control heading rather than using the control law presented in (28)-(30). Furthermore, since the Qualisys system offered positions with very high accuracy, these were used directly as inputs to the control system instead of using an EKF to estimate the vehicle's state. Estimates of linear velocity $\boldsymbol{v}$ for the vehicle were obtained by finding the numerical derivatives of the position estimates.

Figure 8 shows the computer setup and signal flow mapping used in the laboratory studies. The proposed control system, including the elastic band path planner, was implemented in FhSim on the topside computer. Calculated control forces and torques were then transmitted via user diagram protocol (UDP) to the onboard

Table 1: Parameters during laboratory experiments

Parameter	Value	Parameter	Value
k_{int}	0.5	$U_{\min}$	0.05 m/s
k_{ext}	2.5	$U_{\max}$	0.3 m/s
k_{surface}	2.5	t_c	4 s
k_{seafloor}	0	$r_{\max}$	0.4 m
d_{safe}	0.05 m	$r_{\min}$	0.3 m
d_{ol}	0.1 m		

(a) Design parameters

Object	x	y	z	radius
$\boldsymbol{p}_{\text{dock}}$	0.2 m	0.27 m	1 m	
$\boldsymbol{w}_1$	−2 m	−0.8 m	0.25 m	
$\boldsymbol{w}_2$	1.6 m	−0.8 m	0.25 m	
$\boldsymbol{w}_3$	1.6 m	1.2 m	0.25 m	
$\boldsymbol{w}_4$	−2 m	1.2 m	0.25 m	
$\boldsymbol{o}_1$	−1.52 m	−0.69 m	0.24 m	0.2 m
$\boldsymbol{o}_2$	0.64 m	−0.87 m	0.7 m	0.2 m
$\boldsymbol{o}_d$	Varying	Varying	Varying	0.2 m

(b) Positions of obstacles and waypoints

ArduSub software, using the MAVlink (Koubâa et al., 2019) message protocol. Thruster allocation was handled by the onboard ArduSub software, while the vehicle and obstacle positions estimated by Qualisys were transmitted to the topside computer using UDP.

As these experiments served as early testing of our first iteration of the method, some implementation details were based on literature rather than the proposed method in Sections 3-4. First, as suggested by (Lee and Tsai, 2011), instead of Eq. (26), the desired speed calculated by the guidance law was given by

$$U_d(t) = \begin{cases} U_{\max}, & \frac{||\boldsymbol{p}_1 - \boldsymbol{p}||}{t_c} > U_{\max} \\ U_{\min}, & \frac{||\boldsymbol{p}_1 - \boldsymbol{p}||}{t_c} < U_{\min} \\ \frac{||[\boldsymbol{p}_1 - \boldsymbol{p}||}{t_c}, & \text{else}\,, \end{cases} \tag{32}$$

where $t_c > 0$ is a time constant. Furthermore, instead of Eq. (12), the exponent of the repulsive potential (11) was given as

$$D_{\text{aff}} = ||\boldsymbol{p}_i^b - \boldsymbol{p}_j^o|| - r_{\max}\,, \tag{33}$$

similar to (Føre et al., 2021).

The space observed by the Qualisys system determines the positions observable by the system, and thus effectually limits the space for feasible paths in the basin. To avoid having the vehicle ending outside this space, the elastic band path planner was restricted to only alter the desired path along the vertical axis, deviations along the x-y plane could easily lead to coordinates outside the observed volume. This was done by replacing the gradient $\nabla_{\boldsymbol{p}_j}$ in (10) and (13) with the gradient in the z-direction: $\partial/\partial z$. The design parameters of the elastic band path planner and guidance system are given in Table 1a.

5.2.2 Laboratory results

The laboratory experiments featured several case studies to test the basic properties of both the method and the vehicle. Here we only present the results from the most relevant of these, where the ROV had to maneuver an obstacle course with both static and dynamic obstacles. From a starting position $\boldsymbol{p}_{\text{dock}}$, the vehicle was commanded to do three laps around a course defined by the four waypoints $\boldsymbol{w}_1$-$\boldsymbol{w}_4$, before returning to $\boldsymbol{p}_{\text{dock}}$. The course was also fitted with two static obstacles, $\boldsymbol{o}_1$ and $\boldsymbol{o}_2$, that were placed such that the path planner was required to plan a path that ascended above or descended below the obstacles. Furthermore, a third obstacle $\boldsymbol{o}_d$ was used as a dynamic obstacle in that it was lowered into the path ahead of the ROV while it was following its planned path. This forced the path planner to dynamically alter the path to avoid collisions. The placement of waypoints and obstacles and the radius of obstacles are given in Table 1b.

During the experiments, we found that the path planner successfully guided the ROV to the waypoints while avoiding obstacles. Snapshots of the experiment, including the state of the path planner and obstacles can

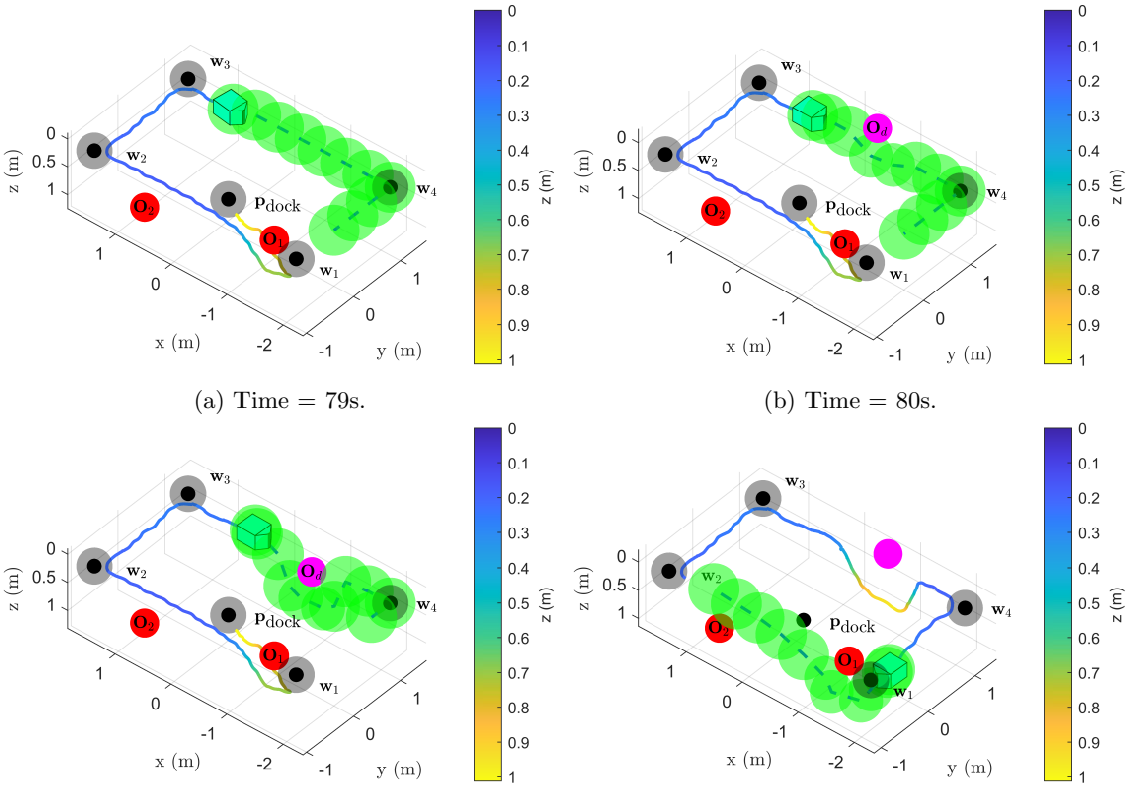

(a) Time = 79s.

(b) Time = 80s.

(c) Time = 82s.

(d) Time = 120s.

Figure 9: Snapshots from a laboratory experiment where the ROV traveled three laps around an obstacle course. The trajectory of the ROV is given with varying colors which specify the depth. Static obstacles are in red and the dynamic obstacle is in magenta.

be seen in Figure 9. The path planner was able to quickly find a new path with respect to the dynamic obstacle, as seen in Figures 9a-9c. We also identified certain situations where the distance between the vehicle and the obstacle was slightly less than the safety margin d_{safe} set by the designer. It was identified that the primary reason for this was that the dynamic obstacle was lowered toward the vehicle at a faster speed than the maximum speed of the vehicle ($U_{\max}$), thus exceeding the natural constraints of the path planning framework. However, this was valuable for identifying necessary changes to the GNC system before field deployment, which included the guidance law and repulsive forces in the elastic band method.

6 Field experiments

This section presents the outcomes of the full-scale field trial that functioned as the final validation of the elastic band method in this study. The experiment was conducted at an industrial-scale fish farm, and we will here describe the setup and configuration of the study, covering elements such as the hardware and software used in the study, and the fish farm that was the venue of the experiments, before presenting the results from case studies. The case studies were planned with gradually increasing difficulty with the aim of a step-wise evaluation of the control framework performance, which incorporated as many tested cases as possible given our time and resources. To validate that the ROV was able to follow a commanded path, we first evaluated the performance of simple waypoint following without obstacles. The second test case involved waypoint following with obstacle avoidance using virtual obstacles to validate that the path planner was able to avoid obstacles in a controlled setup. The third and final test case was waypoint following with a dynamic obstacle in the form of another vehicle intercepting the planned path. The path planner therefore

had to continuously replan its path to avoid the intercepting vehicle. As we were operating in the wave zone in an industrial fish farm, the robustness of the proposed control framework to challenges such as sensor noise, sensor dropouts, and wave-induced disturbances was thoroughly tested.

6.1 Setup and configuration

Argus Mini ROV

Experiments were conducted using an Argus Mini ROV (Figure 10a, to the right), which is a 90 kg observation class ROV developed by the Norwegian company Argus Remote Systems AS (Argus Remote Systems AS., 2023). The vehicle measures $L \times W \times H = 0.9\text{m} \times 0.65\text{m} \times 0.5\text{m}$ in size, and has four horizontal and two vertical electric thrusters (Argus 800W, capable of forces up to 117.5 N) arranged such that the vehicle is actuated in surge, sway, heave, and yaw. Further, the vehicle was fitted with an HD camera, a fluxgate compass for heading measurements, a pressure sensor for depth measurements, a forward-facing Nortek DVL1000 Doppler velocity log (DVL) for velocity measurements, and a gyro for measuring yaw rate. The ROV was also equipped with a Sonardyne Nano transponder to enable 3D position monitoring using a Sonardyne MicroRanger 2 ultra-short baseline (USBL) system. Due to the air-filled swim bladder of salmon, the fish may interfere with the transmission of hydro-acoustic signals, introducing both scattering and multipath, which can limit the performance of the USBL and DVL systems (Rundtop and Frank, 2016). As achieving bottom-lock with the DVL was unlikely in a fully-stocked fish cage, the instrument was rather installed front-facing such that it could lock with the wall of the net pen as the vehicle-wall axis is less likely to be obstructed by fish than the vehicle-bottom axis (Rundtop and Frank, 2016; Amundsen et al., 2022). Despite these measures, the performance of the DVL was severely degraded with large periods of measurement dropouts during the trials.

The ROV was operated using a surface control computer onboard the support vessel M/S Torra (a 14 m research vessel, Figure 10b) through an umbilical that transmits power and control commands back to the ROV. This surface control computer includes an Argus control console with a joystick and automatic heading and depth control which is typically used during normal manual control. The console also features a switch that enables overriding the commands from the control console and rather relaying control signals received through an RS232 port. By attaching a separate control computer to this port, it is then possible to send control commands from an autonomous control system to steer the vehicle, which was done during the trials.

Intercepting vehicle

A BlueROV2 (Figure 10a, in the middle) was used as the intercepting vehicle in the third case study. This vehicle was manually controlled using the QGroundControl graphical user interface (GUI) (Dronecode Project, Inc., 2023) and the ArduSub control system. Since the obstacle avoidance method also required the position of the BlueROV2, it was also fitted with a Sonardyne Nano USBL transponder.

SINTEF ACE Rataren fish farm

The trials took place at Rataren, an industrial-scale salmon farming site outside the coast of the mid of Norway that is part of the SINTEF ACE full-scale laboratory which is a cluster of fish farming sites dedicated to the research and development of aquaculture technology (Figure 10b) (SINTEF, 2023). The site features several net cages that each may contain up to 200 000 salmon at a total biomass of up to 1000 t, and these trials took place during the final ongrowing phase for the salmon, with each individual weighing approximately 5 kg. SINTEF ACE Rataren is located in open waters such that it is exposed to ocean waves and current forces, and the net pens will therefore deform from the sea loads.

Guidance, navigation and control system

In preparation for the trials, the proposed control framework from Section 4 was implemented in FhSim. During operations, the sensor readings from the Argus and the Nortek DVL were transmitted

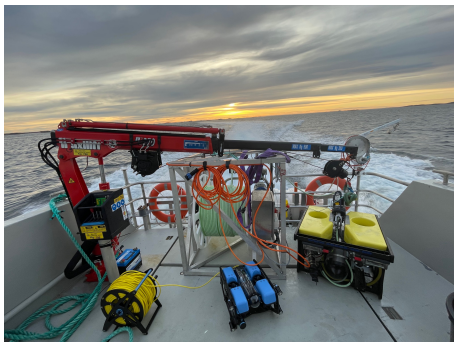

(a) The Argus Mini (yellow) and BlueROV2 (blue) ROVs at the back of the research vessel M/S Torra. Photo: Eleni Kelasidi.

(b) M/S Torra at the SINTEF ACE Rataren fish farm. Photo: Magnus O. Pedersen.

Figure 10: The vehicles and research vessel used during the trials at SINTEF ACE aquaculture laboratory.

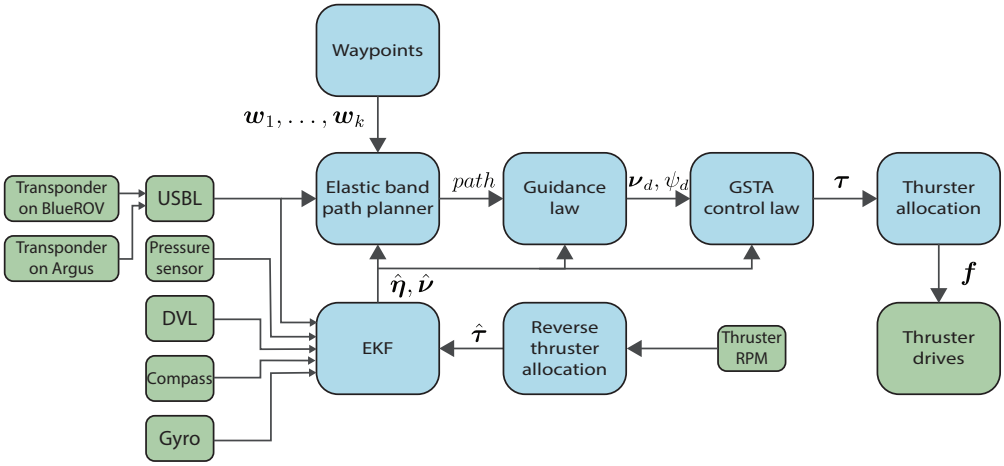

Figure 11: Guidance, navigation and control system during the field experiments. The modules in the blue boxes were implemented in FhSim, while the modules in the green boxes contain the hardware interfaces.

to the topside computer using serial connections, while measurements from the Sonardyne USBL system were transmitted over UDP. The sensor readings were parsed in FhSim, and the measurement vector $\boldsymbol{y} = [x_{\text{usbl}}, y_{\text{usbl}}, z_{\text{pressure}}, \psi_{\text{compass}}, u_{\text{dvl}}, v_{\text{dvl}}, w_{\text{dvl}}, r_{\text{gyro}}]^T$ was directed to the EKF. From waypoints $\boldsymbol{w}_1, \cdots, \boldsymbol{w}_k$, state estimations $\hat{\boldsymbol{\eta}}, \hat{\boldsymbol{\nu}}$, and the measured position of the obstacle vehicle $\boldsymbol{p}_{\text{obstacle}}$, the elastic band path planner and guidance law calculated the reference signals $\boldsymbol{\nu}_d, \psi_d$ for the control system. The GSTA control law calculated the control forces and moments, and, using the control allocation as specified in Appendix A, the thruster forces were calculated and transmitted back to the ROV over serial connection. Figure 11 shows a block diagram of the implemented control framework. The GNC system, including the path planner, ran at a frequency of 10 Hz.

6.2 Results

The parameters of the elastic band path planner and guidance law are given in Table 2, while the parameters of the control law were $\boldsymbol{K}_1 = \text{diag}(0.5, 1, 1, 2), \boldsymbol{K}_2 = \text{diag}(5, 1, 1, 0.008), \boldsymbol{\beta} = \text{diag}(5, 10, 10, 15)$. Further, the parameters of the matrices $\hat{\boldsymbol{M}} = \hat{\boldsymbol{M}}_{RB} + \hat{\boldsymbol{M}}_A, \hat{\boldsymbol{D}}(\hat{\boldsymbol{\nu}})$ and vector $\hat{\boldsymbol{g}}(\hat{\boldsymbol{\eta}})$ of the EKF were chosen similar to the simulation model parameters presented in Appendix A, while the Coriolis and centripetal matrix $\hat{\boldsymbol{C}}(\boldsymbol{\nu})$ was calculated from the mass matrix $\hat{\boldsymbol{M}}$ (Fossen, 2021). The bias time matrix

Table 2: Design parameters of the path planner and guidance system

k_{int}	k_{ext}	k_{surface}	k_{seafloor}	$r_{\min}$	$r_{\max}$	d_{safe}	d_{ol}	$U_{\min}$	$U_{\max}$
4	4	0.3	0	1m	3m	1.5m	1.5m	0.05m/s	0.25m/s

of the EKF was given by $\boldsymbol{T}_b = \text{diag}(100, 100, 100, 100)$, while the process noise matrix was given by $\boldsymbol{E} = \text{diag}(1, 1, 1, 1, 2, 2, 2, 2, 2, 2, 2, 2)$. Finally, the covariance matrices for the process and measurement noises were given by $\boldsymbol{Q} = \text{diag}(0.5, 0.5, 2, 2, 3, 3, 1, 2, 1, 1, 1, 1)$ and $\boldsymbol{R} = \text{diag}(3, 3, 1, 1, 1, 1, 5, 2)$ respectively.

6.2.1 Waypoint following without obstacles

For the first case study, four waypoints were placed in a square pattern at varying depths, and the ROV was commanded to travel one lap. The positions of the waypoints were

$$\boldsymbol{w}_1 = \begin{bmatrix} 8 \\ 15 \\ 2 \end{bmatrix}, \quad \boldsymbol{w}_2 = \begin{bmatrix} 8 \\ 22 \\ 3 \end{bmatrix}, \quad \boldsymbol{w}_3 = \begin{bmatrix} 2 \\ 20 \\ 4 \end{bmatrix}, \quad \boldsymbol{w}_4 = \begin{bmatrix} 4 \\ 12 \\ 3 \end{bmatrix}. \tag{34}$$

The trajectory of the ROV can be seen in Figure 12. As seen in Figure 12a, the elastic band path planner calculates the shortest path consisting of straight lines to the waypoints, while Figure 12b shows that the ROV successfully reaches the waypoints within the acceptance sphere of 1m. Although the update frequency of the USBL measurements varied between intervals of 2 and 6 s, the dead-reckoning of the EKF compensated for this such that the control system was able to maneuver the vehicle along the path. The performance of the control system is shown in Figure 13, which shows that the GSTA controller was able to follow the reference signals, albeit with some oscillations in heave. The oscillating response in the heave velocity could be the result of induced wave forces, as the vehicle is operating in the wave zone.

6.2.2 Obstacle avoidance with virtual obstacles

In the tests with virtual obstacles, the waypoints were placed at the same horizontal positions as in the first test, but all with the same depth of 3 m rather than letting this be variable:

$$\boldsymbol{w}_1 = \begin{bmatrix} 8 \\ 15 \\ 3 \end{bmatrix}, \quad \boldsymbol{w}_2 = \begin{bmatrix} 8 \\ 22 \\ 3 \end{bmatrix}, \quad \boldsymbol{w}_3 = \begin{bmatrix} 2 \\ 20 \\ 3 \end{bmatrix}, \quad \boldsymbol{w}_4 = \begin{bmatrix} 4 \\ 12 \\ 3 \end{bmatrix}. \tag{35}$$

Two static obstacles were programmed with parameters

$$\boldsymbol{O}_1 = \begin{bmatrix} \boldsymbol{p}_1^o \\ r_1^o \end{bmatrix} = \begin{bmatrix} 8 \\ 19 \\ 2 \\ 1 \end{bmatrix}, \quad \boldsymbol{O}_2 = \begin{bmatrix} \boldsymbol{p}_2^o \\ r_2^o \end{bmatrix} = \begin{bmatrix} 3 \\ 15 \\ 4 \\ 1 \end{bmatrix}. \tag{36}$$

The positions of the obstacles were such that the ROV had to dive below $\boldsymbol{O}_1$ to reach $\boldsymbol{w}_2$ and ascend above $\boldsymbol{O}_2$ to reach $\boldsymbol{w}_4$.

The trajectory of the ROV during the case study can be seen in Figure 14, demonstrating that the ROV reached the waypoints while diving underneath $\boldsymbol{O}_1$ and ascending above $\boldsymbol{O}_2$. Figures 14a-14b show that the bubbles were placed such that the path stayed within the free-space. The performance of the control system is seen in Figure 15, which shows a very good performance by the GSTA controller. The distance between the vehicle and the obstacles can also be seen in Figure 15, where it is clear that the vehicle did not collide with the virtual obstacles.

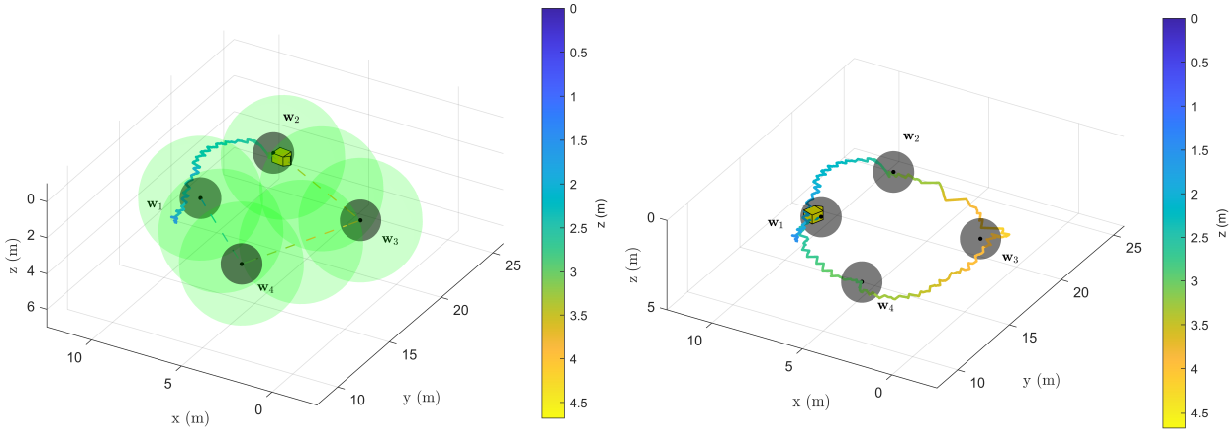

(a) Snapshot, including the state of the elastic band, after 60s.

(b) Trajectory at completion.

Figure 12: Trajectory of ROV during waypoint following without obstacles. The color variation of the trajectory reflects variation in vehicle depth; a deeper blue signals a shallow depth and yellow signals a deeper depth.

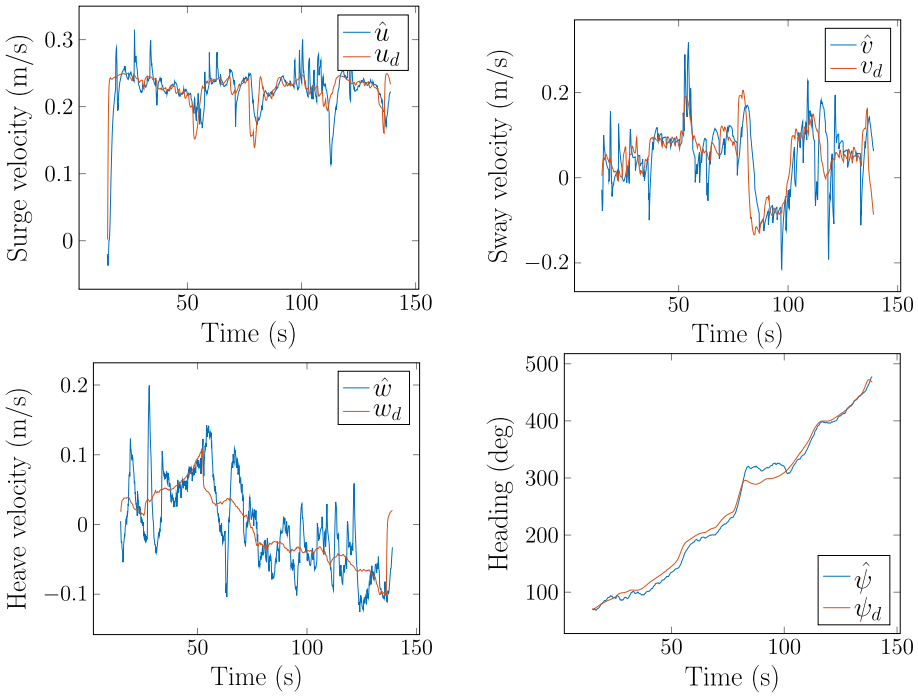

Figure 13: Reference tracking during waypoint following without obstacles.

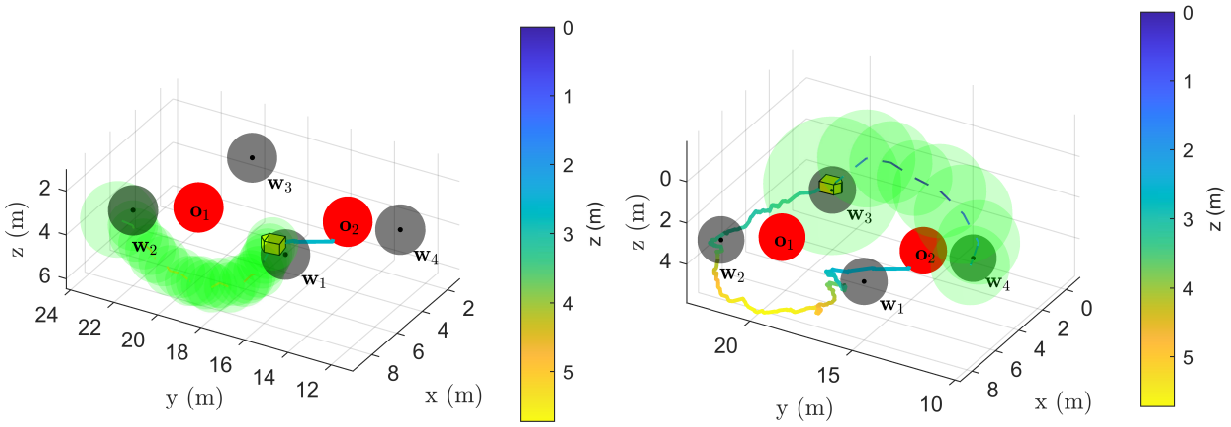

(a) Snapshot after 10s, including the bubbles on the elastic band up to $\boldsymbol{w}_2$.

(b) Snapshot after 120s, including the bubbles on the elastic band up to $\boldsymbol{w}_4$.

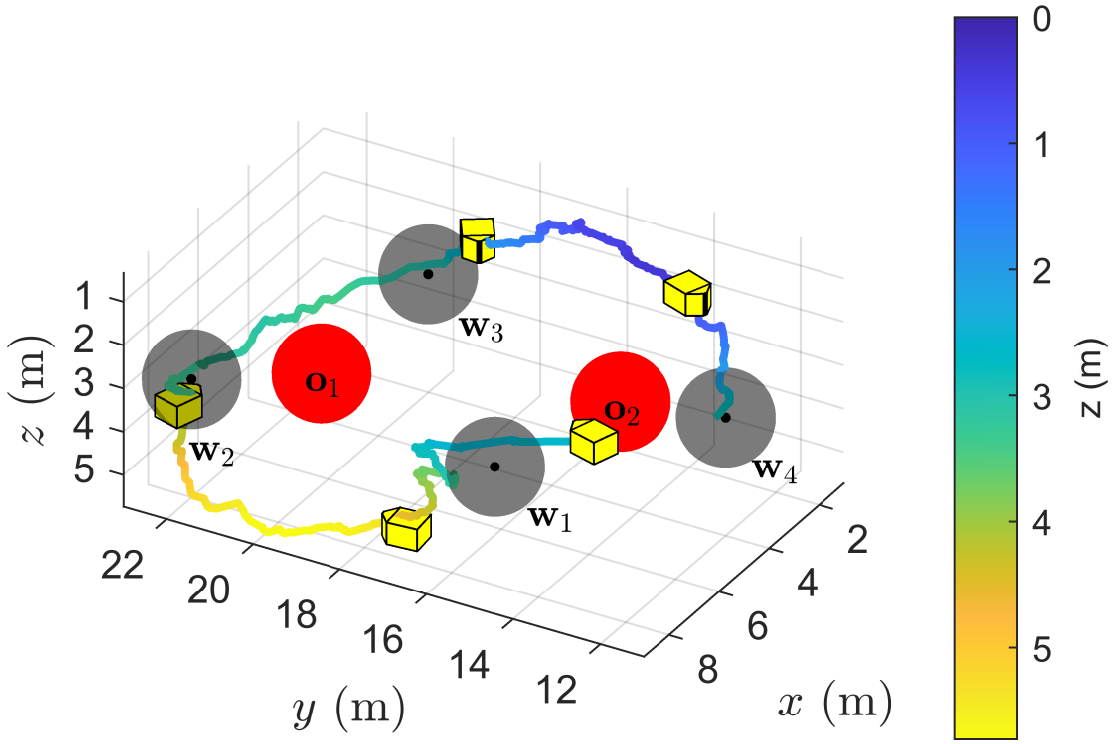

(c) Trajectory at completion.

Figure 14: Trajectory of ROV during waypoint following with virtual obstacles. The color variation in trajectory reflects variation in vehicle depth; a deeper blue signals a shallow depth and yellow signals a deeper depth.

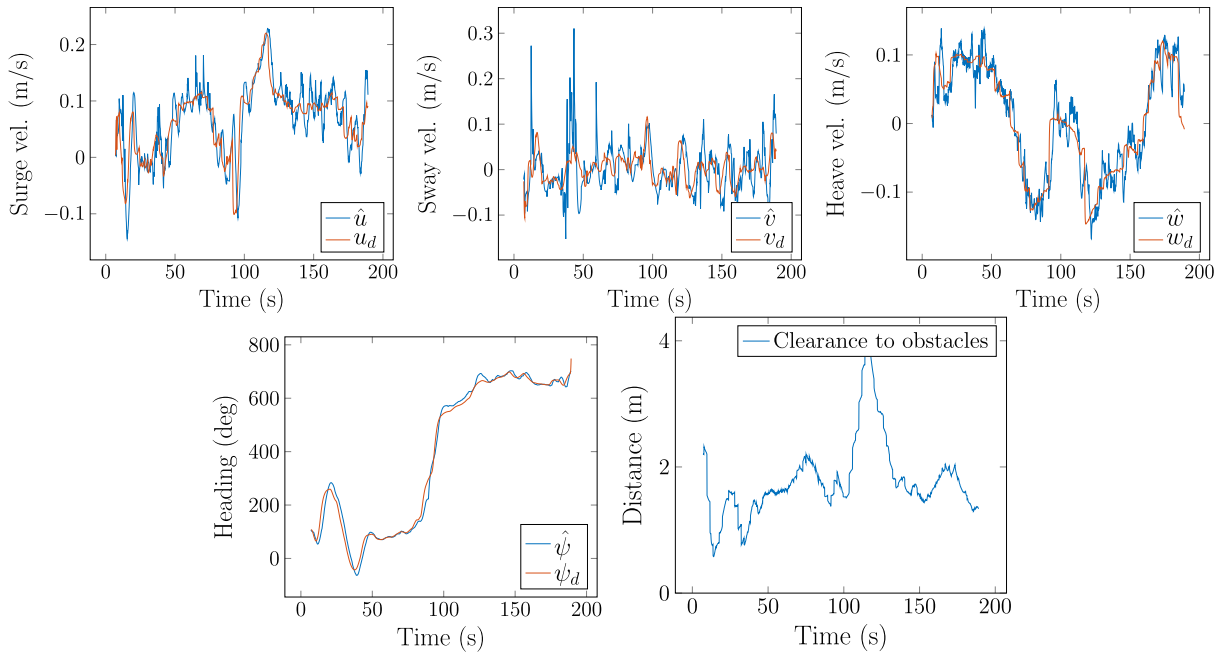

Figure 15: Reference tracking and obstacle clearance during waypoint following with virtual obstacles.

6.2.3 Obstacle avoidance with intercepting vehicle

In the final case study, the objective was for the ROV to travel from the waypoint $\boldsymbol{w}_1 = [-3.5, 5.2, 1]^T$ to the waypoint $\boldsymbol{w}_2 = [2.7, 19.4, 0]^T$, while avoiding collisions with the intercepting BlueROV2 vehicle. The BlueROV2 was programmed as an obstacle $\mathbf{O}_d$ with a dynamic position and a one-meter radius whose position was measured with a second USBL transponder. As the BlueROV2 did not have a state estimator to perform dead reckoning, a zero-order hold was used to combine the USBL measurements. The intercept operation was facilitated by manually piloting the BlueROV2 into the Argus's path, such that the Argus had to dive below the BlueROV2 and then ascend to reach $\boldsymbol{w}_2$.

The trajectory of the Argus can be seen in Figure 16, showing that the ROV has to dive to avoid colliding with the obstacle vehicle after which it then ascends to reach the goal position successfully. Figure 17 includes combinations of the state of the elastic band and screenshots of a simultaneous video taken from a third ROV. It can clearly be seen that the elastic band deforms to avoid collisions with the obstacle vehicle. Figure 18 shows that the control system was able to track the reference signals and that the ROV kept a safe distance from the obstacle vehicle.

7 Discussion

Autonomous navigation in cluttered and changing underwater environments remains a challenging problem to solve. The problem consists of several parts, such as 3D path planning, robust and precise motion control in the presence of sea loads, and pose estimation and perception when the performance of several sensor types can be degraded. In our research, we have targeted local and reactive path planning and obstacle avoidance with real-time capabilities, with a special emphasis on applications in aquaculture. In this section, we will discuss the key findings of this research, the challenges that we faced, and future work and prospects.

Through extensive studies in situations, laboratory experiments, and sea trials, we found that the elastic band is a viable candidate for fast path planning and obstacle avoidance in environments that are quickly

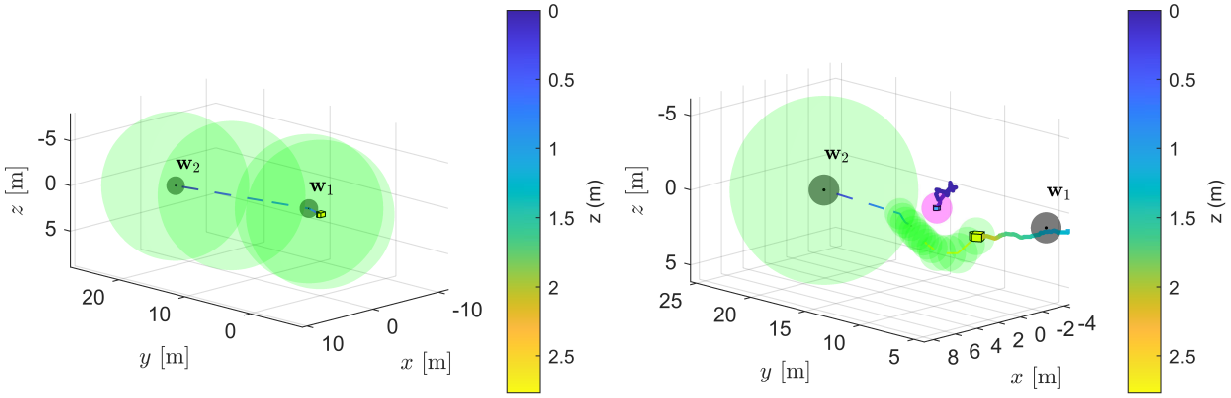

(a) Snapshot at 0s.

(b) Snapshot at 40s.

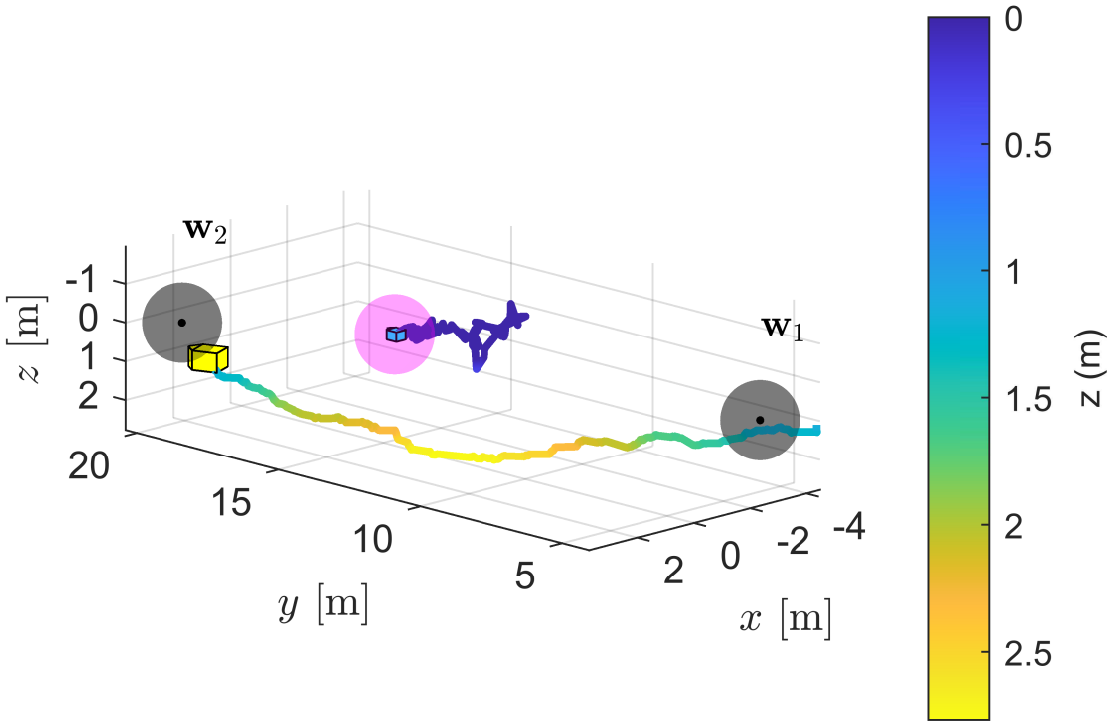

(c) Trajectory at completion.

Figure 16: Trajectory of the Argus Mini (yellow) during obstacle avoidance with obstacle vehicle (blue). The color variation in trajectory reflects variation in vehicle depth; a deeper blue signals a shallow depth and yellow signals a deeper depth.

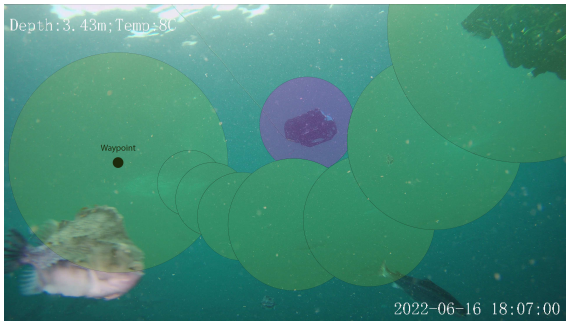

(a) Time = 30s.

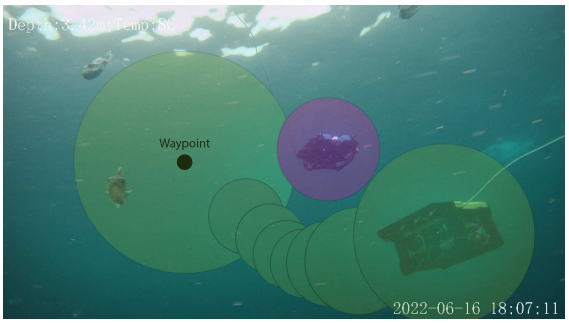

(b) Time = 40s.

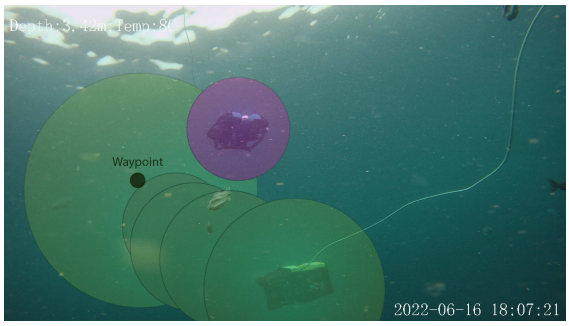

(c) Time = 50s.

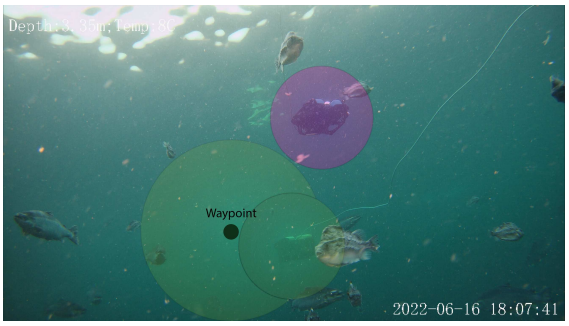

(d) Time = 70s.

Figure 17: Obstacle avoidance with an intercepting vehicle acting as a dynamic obstacle. The state of the elastic band is rendered on top of video screenshots.

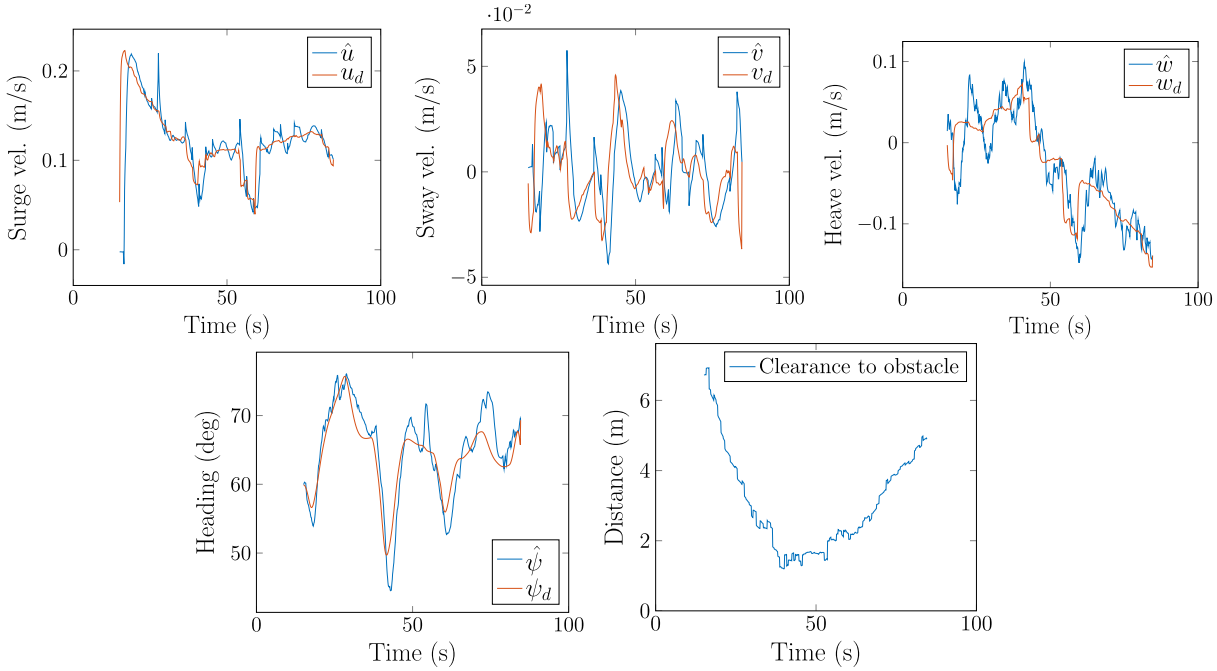

Figure 18: Reference tracking and obstacle clearance during dynamic obstacle avoidance.

changing. The method proved to plan paths that avoided moving obstacles with a planning update frequency of fractions of a second. Further, modeling the dynamics of the path as a physical system has its advantages, as it is easy for humans to conceptualize the internal mechanics of the planner. While the method requires the tuning of several parameters, they all have a basis in physics and a close resemblance to the tuning of familiar control concepts such as proportional-integral-derivative (PID) control, making the tuning fairly intuitive.

In our research, we utilized that the ROV was actuated in 4DOFs such that we were able to control it to quickly change direction in all three translation axes. Many underwater vehicles, such as torpedo-shaped AUVs, are not actuated in sway and heave, which puts constraints on the paths that they can follow. For such systems, the elastic band path planner may produce paths that are infeasible for the vehicle. A potential improvement to the method can therefore be to include extensions that consider the dynamics of the vehicle, which should ensure that the produce paths are feasible. It should be mentioned, however, that this forces the method to be tailored to the vehicle, thus making it difficult to quickly transfer the method between different systems.

Another extension to the method could be to also consider the velocity and potential future states of obstacles. An intuitive way to include this is to make changes to the repulsive field generated by obstacles, as suggested in (Lee and Tsai, 2011), or by considering the swept-out volumes of moving obstacles (Amundsen et al., 2024). Further, this problem also includes the problem of target tracking of the obstacles, which might enable more sophisticated methods to model the future state of obstacles as suggested by (Rothmund et al., 2022). Another prospect is to enable obstacles of varying shapes. The current formulation of the generated repulsive field from obstacles assumes that the volume occupied by the obstacle can be represented as a sphere, which works sufficiently for simple shapes but does not encapsulate slender or more complex shapes. A reformulation of the generated repulsive field would require that one is able to accurately measure the shortest distance between the obstacle and the vehicle, as the repulsive force from the obstacle will be decided by this.

As the elastic band models the path as a dynamic system, the new configuration of the path is found by searching for a configuration where the system is in equilibrium. In our implementation, we have solved this by the use of gradient descent iteratively through each bubble. This proved to efficiently find solutions close to equilibria. However, there is no guarantee that the method will find an exact solution and the computation efficiency decreases as the required number of bubbles increases. We found in our research that the performance of the method is highly dependent on choices of parameters and imprecise tuning can lead to scenarios where the position and radius of bubbles may oscillate between timesteps, which can introduce challenges to the control system. A better way of solving the set of dynamic equations may therefore improve the overall performance of the method.

The method is inspired by potential fields and therefore shares some of the pros and cons of potential fields. In our testing, we found that the method was quickly able to find short and safe paths to waypoints, but, as the repositioning of bubbles follows valleys in their potential fields, the method will not generally be able to find local optimal solutions quickly if the bubbles' potential fields do not lead them towards optimal positions. In scenarios where the normal vectors from obstacles lead away from the optimal path, the path planner will be unable to find this solution, and, more critically, if the bubbles' potential field does not lead toward a feasible solution, the path planner may not be able to find a solution at all. In such scenarios, it will be important to combine the elastic band path planner with a global path planner that can find an optimal path (Wang et al., 2020) and have a fall-back approach in cases where it is not able to quickly find a feasible path.

Another interesting point is the similarities between the method and that of optimal control theory, as first mentioned by (Quinlan, 1994). In fact, it can be shown that if one is to use optimization theory to minimize the length of a path, the minimum point of the cost function has great similarities to the equilibrium condition of the elastic band path planner (the only difference being a scalar gain). This point would suggest that the paths calculated by the elastic band path planner will often be close to the shortest path. It would be

interesting to further study the similarities between the two approaches.

In our field experiments, we tested the method in a fully stocked fish cage. This is a difficult terrain for navigation systems. Firstly, hydro-acoustic sensors are prone to dropouts and measurement errors because the fish may lead to scattering or multipath propagation effects of the hydroacoustic signals. Secondly, water turbidity and a lack of clear landmarks due to the fish schools blocking the field-of-view (FOV) of the camera may degrade the performance of visual-based pose estimation methods. Lastly, the high signal attenuation in water makes several sensors commonly used in terrestrial applications unavailable, including GNSS and LIDARs. In our navigation system, we relied on internal sensors (compass, pressure sensor, and gyro), as well as a DVL and a USBL system. We found that both of these hydroacoustic sensors were affected by the fish. Particularly, this was the case for the DVL, which had longer dropout periods. As our EKF was based on a sophisticated model of the vehicle, it was able to provide a good state estimation, even in periods without position or velocity measurements. However, errors will naturally grow over time as integration is greatly affected by biases and noise. Therefore, it could be observed that the state estimation made big corrections when new USBL measurements arrived after long dropout periods. Further improvements to the navigation system and sensor suite should be able to provide more reliable state estimations, for instance, better tuning of the EKF, sophisticated outlier detection modules to compensate for measurement errors, or, if high-rate IMU measurements were available, formulate the EKF in an error-state form (Solà, 2017).

7.1 Future prospects

The research presented in this paper is part of a greater research goal, namely providing autonomy in dynamically changing environments. The path planner presented is able to quickly calculate safe and short paths within a limited space, but is, like most local path planners, prone to getting stuck in local minima as they only consider a limited scope of information. Future work for us is, therefore, to combine the elastic band path planner with a global path planner, where the global path planner should be able to find feasible paths, while the elastic band path planner will quickly react to changes in the environment to avoid collisions.

To further be equipped to handle the challenges of dynamic environments with fast-moving obstacles, we are looking into extending the method by incorporating the velocity space of obstacles, for instance by employing the approach suggested in Amundsen et al. (2024). Furthermore, to be robust to state uncertainty, either from unmodeled dynamics, noisy measurements, or poor control performance, we take inspiration from works such as Majumdar and Tedrake (2017), Chen et al. (2021), and Xanthidis et al. (2023) and aim to formulate an extension where the radii of bubbles and their overlap change dynamically in accordance with the system state uncertainty. Finally, we want to make modifications to the artificial forces to enforce path smoothness between the sub-paths connected at waypoints.

In our field experiments, we measured the position of obstacles using a USBL system. However, in a practical scenario, the position of obstacles must be measured using the vehicle's sensors. Therefore, obstacle detection remains future work for us, either by using visual-based methods (Kelasidi et al., 2019) or hydroacoustic sensors such as multibeam sonars(Cao et al., 2023).

In our simulation studies, we studied one example of how the elastic band can be used to navigate a fish farm, taking into account the position and geometry of the fish cage. However, we were unable to test this in field experiments, as the position and geometry of the fish cage were unknown to us. Further testing of this is left for future work, where for instance the net cage shape can be measured with acoustic tags (Kelasidi et al., 2022; Su et al., 2021; Haugaløkken et al., 2018), DVL (Amundsen et al., 2022) or sonars (Cardaillac et al., 2023). Common operations with ROVs in aquaculture are inspection and cleaning operations of the nets, in which the ROV must keep a fixed distance to the net. In such a scenario it can be considered to use the elastic band path planner in a different context where the net also applies an attracting force to the path.

Finally, many UUV operations in aquaculture, such as net inspection and cleaning, rely on knowing which part of the net cage has been traversed. Simultaneous localization and mapping methods that both estimate

the state of the vehicle and map the inspected sections of the structure are therefore very attractive, as this will provide information about both the vehicle and structure. This is also something we would like to investigate in the future.

8 Conclusion

Raising the autonomy level for UUV operations in complex underwater environments that are changing in time and space puts several requirements on the vehicle control systems. In our work, we have studied fast path planning and obstacle avoidance in a dynamically changing 3D space. Particularly, this paper has presented an obstacle avoidance and path planning framework for UUVs based on the elastic band method. Through simulations, laboratory experiments, and sea trials, we have shown that the path planning framework can guide the vehicle to reach waypoints in the presence of moving obstacles and non-fixed spatial constraints. We have had a special emphasis on aquaculture operations, as this is the domain in which we apply our research, but presented the methods in a more general setting to make it relevant for other industries. The proposed control framework has been demonstrated using two underwater robotic platforms showing the validity of the proposed work and its applicability to a wide range of subsea applications and UUV platforms. In the field experiments, we applied the path planner framework on an ROV operating in a full-scale aquaculture fish farm, which successfully demonstrated the performance of the system. The results, the intuitiveness of the method, and its real-time performance suggest that the elastic band method is a viable method for underwater obstacle avoidance in dynamically changing environments.

In summary, in all the investigated case studies the proposed method managed to quickly and efficiently plan paths that enabled collision-free navigation, also in the presence of moving obstacles and spatial constraints. While the deployment of fully autonomous control systems for UUVs in dynamically changing environments requires further components, this research supports this development and demonstrates that this is within the grasp of the robotic research community.

Appendix A

The system inertia matrix of the vehicle simulation model, consisting of the rigid-body mass matrix $\boldsymbol{M}_{RB}$ and the added mass matrix $\boldsymbol{M}_A$, is given by

$$\boldsymbol{M} = \boldsymbol{M}_{RB} + \boldsymbol{M}_A = \begin{bmatrix} 90 & 0 & 0 & 0 \\ 0 & 90 & 0 & 0 \\ 0 & 0 & 90 & 0 \\ 0 & 0 & 0 & 13 \end{bmatrix} + \begin{bmatrix} 54 & 0 & 0 & 0 \\ 0 & 72 & 0 & 0 \\ 0 & 0 & 360 & 0 \\ 0 & 0 & 0 & 5.2 \end{bmatrix} = \begin{bmatrix} 144 & 0 & 0 & 0 \\ 0 & 162 & 0 & 0 \\ 0 & 0 & 450 & 0 \\ 0 & 0 & 0 & 18.2 \end{bmatrix},$$

while the damping matrix is given by

$$\boldsymbol{D}(\boldsymbol{\nu}) = \begin{bmatrix} 250 + 350|u| & 0 & 0 & 0 \\ 0 & 200 + 350|v| & 0 & 0 \\ 0 & 0 & 175 + 400|w| & 0 \\ 0 & 0 & 0 & 15 + 75|r| \end{bmatrix}.$$

The Coriolis and centripetal matrix can be calculated from $\boldsymbol{M}$ according to

$$\boldsymbol{C}(\boldsymbol{\nu}) = \begin{bmatrix} 0 & 0 & 0 & 162v \\ 0 & 0 & 0 & -144u \\ 0 & 0 & 0 & 0 \\ -162v & 144u & 0 & 0 \end{bmatrix},$$

and the vector of gravitational and buoyancy forces is given by

$$\boldsymbol{g}(\boldsymbol{\eta}) = \begin{bmatrix} 0 \\ 0 \\ -0.91 \\ 0 \end{bmatrix}.$$

Units are given in SI.

The forces and moments from the ocean current are given according to

$$\boldsymbol{\tau}_c = \boldsymbol{C}(\boldsymbol{\nu}_c)\boldsymbol{\nu}_c + \boldsymbol{D}(\boldsymbol{\nu}_c)\boldsymbol{\nu}_c$$

where $\boldsymbol{\nu}_c$ is the velocity of the ocean current in the body-fixed frame, while the wave excitation forces are calculated according to the generalized Morrison's equation for small-volume structures (Faltinsen, 1990)

$$\boldsymbol{\tau}_w = \left(\frac{B}{W}\boldsymbol{M}_{RB} + \boldsymbol{M}_A\right)\dot{\boldsymbol{\nu}}_w$$

where $\dot{\boldsymbol{\nu}}_w = [\dot{u}_w, \dot{v}_w, \dot{w}_w, 0]^T$ is the water acceleration at $\boldsymbol{p}$. The current and wave model implementations are based on the SINMOD oceanographic model (Slagstad and McClimans, 2005).

The thruster allocation has the form

$$\boldsymbol{\tau} = \boldsymbol{B}\boldsymbol{f}$$

where the thruster allocation matrix is

$$\boldsymbol{B} = \begin{bmatrix} \cos(35^\circ) & \cos(35^\circ) & \cos(35^\circ) & \cos(35^\circ) & 0 & 0 \\ \sin(35^\circ) & -\sin(35^\circ) & -\sin(35^\circ) & \sin(35^\circ) & 0 & 0 \\ 0 & 0 & 0 & 0 & 1 & 1 \\ b_1 & b_2 & b_3 & b_4 & 0 & 0 \end{bmatrix},$$

with

$$\begin{aligned} b_1 &= 0.216\cos(35^\circ) + 0.202\sin(35^\circ), \\ b_2 &= -0.216\cos(35^\circ) + 0.202\sin(35^\circ), \\ b_3 &= 0.265\cos(35^\circ) - 0.195\sin(35^\circ), \\ b_4 &= -0.265\cos(35^\circ) - 0.195\sin(35^\circ), \end{aligned}$$

and the thruster vector is

$$\boldsymbol{f} = \begin{bmatrix} f_1 & f_2 & f_3 & f_4 & f_5 & f_6 \end{bmatrix}^T.$$

The distributed control forces can be found by solving

$$\boldsymbol{f} = \boldsymbol{B}^T\left(\boldsymbol{B}\boldsymbol{B}^T\right)^{-1}\boldsymbol{\tau}.$$

The control forces of each thruster are saturated according to

$$\bar{f}_i = \max\left(-85, \min(f_i, 117.5)\right),$$

and their rate is limited according to

$$y_{i_k} = \begin{cases} 1.5\left(t_k - t_{k-1}\right) + y_{i_{k-1}}, & \frac{\bar{f}_{i,k} - y_{i_{k-1}}}{t_k - t_{k-1}} \geq 1.5 \\ -1.5\left(t_k - t_{k-1}\right) + y_{i_{k-1}}, & \frac{\bar{f}_{i,k} - y_{i_{k-1}}}{t_k - t_{k-1}} \leq 1.5 \\ \bar{f}_{i,k}, & \text{else}, \end{cases}$$

where t_k is the time at step k, $\bar{f}_i$ is the commanded input of thruster i at step k, and y_{i_k} is the output at step k.

Appendix B

A video file is included as an appendix to this work. The video contains recordings of the simulations and field experiments presented in this work. The video is also available at `https://youtu.be/rIwrpKp4HnQ`.

Acknowledgments

The work presented in this publication is supported by the Research Council of Norway (RCN) projects CHANGE (RCN project no. 313737) and NetClean 24/7 (RCN project no. 296392). The authors would like to thank SINTEF ACE and Kay Arne Skarpnes for their support in this project. The authors would also like to thank Sverre Fjæra, who, through his master's thesis, helped develop the methods in this paper.

References

Ames, A. D., Coogan, S., Egerstedt, M., Notomista, G., Sreenath, K., and Tabuada, P. (2019). Control barrier functions: Theory and applications. In *Proc. 18th European Control Conference (ECC)*, pages 3420–3431.

Amundsen, H. B., Caharija, W., and Pettersen, K. Y. (2022). Autonomous ROV inspections of aquaculture net pens using DVL. *IEEE J. Oceanic Eng.*, 47:1–19.

Amundsen, H. B., Olsen, T. F., Xanthidis, M., Føre, M., and Kelasidi, E. (2024). RUMP: Robust underwater motion planning in dynamic environments of fast moving obstacles. In *IEEE International Conference on Robotics and Automation (ICRA)*. Accepted.

Antonelli, G. (2018). *Underwater Robots*. Springer.

Argus Remote Systems AS. (2023). Argus Mini. `https://www.argus-rs.no/argus-rovs/11/argus-mini`. Accessed: 2023-01-04.

Balchen, J. G. (1991). Possible roles of remotely operated underwater vehicles (ROV) and robotics in mariculture of the future. *Modeling, Identification and Control*, 12:207–217.

Bansal, S., Chen, M., Herbert, S., and Tomlin, C. J. (2017). Hamilton-Jacobi reachability: A brief overview and recent advances. In *2017 IEEE 56th Annual Conference on Decision and Control (CDC)*, pages 2242–2253.

Blue Robotics, Inc. (2022a). ArduSub. `https://www.ardusub.com/`. Accessed: 2022-12-23.

Blue Robotics, Inc. (2022b). BlueROV2. `https://bluerobotics.com/store/rov/bluerov2/`. Accessed: 2022-12-23.

Brandt, T. and Sattel, T. (2005). Path planning for automotive collision avoidance based on elastic bands. *IFAC Proceedings Volumes*, 38(1):210–215.

Breivik, M. and Fossen, T. (2005). Principles of guidance-based path following in 2D and 3D. In *Proc. 44th IEEE Conference on Decision and Control*, pages 627–634.

Candeloro, M., Sørensen, A. J., Longhi, S., and Dukan, F. (2012). Observers for dynamic positioning of ROVs with experimental results. *IFAC Proceedings Volumes*, 45(27):85–90.

Canny, J. and Reif, J. (1987). New lower bound techniques for robot motion planning problems. In *Proc. 28th Annual Symposium on Foundations of Computer Science*, page 49–60.

Cao, X., Ren, L., and Sun, C. (2023). Research on obstacle detection and avoidance of autonomous underwater vehicle based on forward-looking sonar. *IEEE Transactions on Neural Networks and Learning Systems*, 34(11):9198–9208.

Cardaillac, A., Amundsen, H. B., Kelasidi, E., and Ludvigsen, M. (2023). Application of maneuvering based control for autonomous inspection of aquaculture net pens. In *2023 8th Asia-Pacific Conference on Intelligent Robot Systems (ACIRS)*, pages 44–51.

Castillo, I., Fridman, L., and Moreno, J. A. (2018). Super-twisting algorithm in presence of time and state dependent perturbations. *International Journal of Control*, 91(11):2535–2548.

Chen, M., Herbert, S. L., Hu, H., Pu, Y., Fisac, J. F., Bansal, S., Han, S., and Tomlin, C. J. (2021). FaSTrack: A modular framework for real-time motion planning and guaranteed safe tracking. *IEEE Transactions on Automatic Control*, 66(12):5861–5876.

Diamant, R., Campagnaro, F., de Filippo de Grazia, M., Casari, P., Testolin, A., Sanjuan Calzado, V., and Zorzi, M. (2017). On the relationship between the underwater acoustic and optical channels. *IEEE Transactions on Wireless Communications*, 16(12):8037–8051.

Dronecode Project, Inc. (2023). QGroundControl. `http://qgroundcontrol.com/`. Accessed: 2023-01-02.

Faltinsen, O. M. (1990). *Sea Loads on Ships and Offshore Structures*. Cambridge Ocean Technology. Cambridge University Press.

Fiorini, P. and Shiller, Z. (1998). Motion planning in dynamic environments using velocity obstacles. *The International Journal of Robotics Research*, 17(7):760–772.

Fossen, T. I. (2021). *Handbook of Marine Craft Hydrodynamics and Motion Control*. John Wiley & Sons Ltd.

Fox, D., Burgard, W., and Thrun, S. (1997). The dynamic window approach to collision avoidance. *IEEE Robotics Automation Magazine*, 4(1):23–33.

Føre, H. M. and Thorvaldsen, T. (2021). Causal analysis of escape of atlantic salmon and rainbow trout from norwegian fish farms during 2010–2018. *Aquaculture*, 532:736002.

Føre, M., Fjæra, S., Ohrem, S. J., Kelasidi, E., Bloecher, N., and Amundsen, H. B. (2021). Adaptive motion planning and path following for permanent resident biofouling prevention robot operating in fish farms. In *Proc. IEEE/MTS OCEANS*, pages 1–10.

Føre, M., Frank, K., Norton, T., Svendsen, E., Alfredsen, J. A., Dempster, T., Eguiraun, H., Watson, W., Stahl, A., Sunde, L. M., Schellewald, C., Skøien, K. R., Alver, M. O., and Berckmans, D. (2018). Precision fish farming: A new framework to improve production in aquaculture. *Biosystems Engineering*, 173:176 – 193.

Gansel, L. C., Rackebrandt, S., Oppedal, F., and McClimans, T. A. (2014). Flow fields inside stocked fish cages and the near environment. *Journal of Offshore Mechanics and Arctic Engineering*, 136.

Hanafusa, H., Yoshikawa, T., and Nakamura, Y. (1981). Analysis and control of articulated robot arms with redundancy. *IFAC Proceedings Volumes*, 14(2):1927–1932. 8th IFAC World Congress on Control Science and Technology for the Progress of Society, Kyoto, Japan, 24-28 August 1981.

Haugaløkken, B. O. A., Sandøy, S. S., Schjølberg, I., Alfredsen, J. A., and Utne, I. B. (2018). Probabilistic localization and mapping of flexible underwater structures using octomap. In *Proc. European Control Conference (ECC)*, pages 268–275.

Haugaløkken, B. O. A., Amundsen, H. B., Fadum, H. S., Gravdahl, J. T., and Ohrem, S. J. (2023). Adaptive generalized super-twisting tracking control of an underwater vehicle. In *Proc. IEEE Conference on Control Technology and Applications (CCTA)*, pages 687–693.

Holen, S. M., Utne, I. B., Holmen, I. M., and Aasjord, H. (2018). Occupational safety in aquaculture – part 2: Fatalities in Norway 1982–2015. *Marine Policy*, 96:193–199.

IMO (1972). *Convention on the International Regulations for Preventing Collisions at Sea (COLREGs)*. Internaional Maritime Organization (IMO), London, UK.

Jenie, Y., Van Kampen, E.-J., De Visser, C., Ellerbroek, J., and Hoekstra, J. (2016). Three-dimensional velocity obstacle method for uncoordinated avoidance maneuvers of unmanned aerial vehicles. *Journal of Guidance, Control, and Dynamics*, 39:1–12.

Johansen, T. A. and Fossen, T. I. (2013). Control allocation - a survey. *Automatica*, 49:1087–1103.

Johansen, T. A., Perez, T., and Cristofaro, A. (2016). Ship collision avoidance and COLREGS compliance using simulation-based control behavior selection with predictive hazard assessment. *IEEE Transactions on Intelligent Transportation Systems*, 17(12):3407–3422.

Kelasidi, E., Moe, S., Pettersen, K. Y., Kohl, A. M., Liljebäck, P., and Gravdahl, J. T. (2019). Path following, obstacle detection and obstacle avoidance for thrusted underwater snake robots. *Frontiers in Robotics and AI*, 6.

Kelasidi, E., Su, B., Caharija, W., Føre, M., Pedersen, M., and Frank, K. (2022). Autonomous monitoring and inspection operations with UUVs in fish farms. *IFAC-PapersOnLine*, 55(31):401–408.

Kelasidi, E. and Svendsen, E. (2022). Robotics for sea-based fish farming. In Zhang, Q., editor, *Encyclopedia of Smart Agriculture Technologies*, pages 1–20, Cham. Springer International Publishing.

Khatib, O. (1985). Real-time obstacle avoidance for manipulators and mobile robots. In *Proc. IEEE International Conference on Robotics and Automation*, pages 500–505.

Klebert, P., Øystein Patursson, Endresen, P. C., Rundtop, P., Birkevold, J., and Rasmussen, H. W. (2015). Three-dimensional deformation of a large circular flexible sea cage in high currents: Field experiment and modeling. *Ocean Engineering*, 104:511 – 520.

Koren, Y. and Borenstein, J. (1991). Potential field methods and their inherent limitations for mobile robot navigation. In *Proc. IEEE International Conference on Robotics and Automation*, pages 1398 – 1404.

Koubâa, A., Allouch, A., Alajlan, M., Javed, Y., Belghith, A., and Khalgui, M. (2019). Micro air vehicle link (MAVlink) in a nutshell: A survey. *IEEE Access*, 7:87658–87680.

Kyo, M., Hiyazaki, E., Tsukioka, S., Ochi, H., Amitani, Y., Tsuchiya, T., Aoki, T., and Takagawa, S. (1995). The sea trial of "KAIKO", the full ocean depth research ROV. In *'Challenges of Our Changing Global Environment'. Proc. OCEANS '95 MTS/IEEE*, pages 1991–1996.

LaValle, S. M. (1998). Rapidly-exploring random trees : a new tool for path planning. *The annual research report*.

LaValle, S. M. (2006). *Planning Algorithms*. Cambridge University Press.

Lee, C. H. (1995). WAMIT theory manual. Technical Report MIT Report 95-2, Dept. of Ocean Eng., MIT.

Lee, C.-T. and Tsai, C.-C. (2011). 3D collision-free trajectory generation using elastic band technique for an autonomous helicopter. In Li, T.-H. S., Tu, K.-Y., Tsai, C.-C., Hsu, C.-C., Tseng, C.-C., Vadakkepat, P., Baltes, J., Anderson, J., Wong, C.-C., Jesse, N., Kuo, C.-H., and Yang, H.-C., editors, *Next Wave in Robotics*, pages 34–41. Springer Berlin Heidelberg.

Lemaréchal, C. (2012). Cauchy and the gradient method. *Documenta Mathematica*, pages 251–254.

Majumdar, A. and Tedrake, R. (2017). Funnel libraries for real-time robust feedback motion planning. *The International Journal of Robotics Research*, 36(8):947–982.

Moe, S., Pettersen, K. Y., and Gravdahl, J. T. (2020). Set-based collision avoidance applications to robotic systems. *Mechatronics*, 69:102399.

Nguyen, Q., Hereid, A., Grizzle, J. W., Ames, A. D., and Sreenath, K. (2016). 3D dynamic walking on stepping stones with control barrier functions. In *Proc. IEEE 55th Conference on Decision and Control (CDC)*, pages 827–834.

NTNU (2022). Marine Cybernetics Laboratory. `https://www.ntnu.edu/imt/lab/cybernetics`. Accessed: 2022-12-23.

Ohrem, S. J., Amundsen, H. B., Caharija, W., and Holden, C. (2022). Robust adaptive backstepping DP control of ROVs. *Control Engineering Practice*, 127:105282.

Petillot, Y. R., Antonelli, G., Casalino, G., and Ferreira, F. (2019). Underwater robots: From remotely operated vehicles to intervention-autonomous underwater vehicles. *IEEE Robotics & Automation Magazine*, 26(2):94–101.

Qualisys AB (2022). Qualisys. `https://www.qualisys.com/`. Accessed: 2022-12-23.

Quinlan, S. (1994). *Real-time modification of collision-free paths*. PhD thesis, Stanford University.

Quinlan, S. and Khatib, O. (1993). Elastic bands: connecting path planning and control. In *Proc. IEEE International Conference on Robotics and Automation*, pages 802–807.

Raja, P. and Pugazhenthi, S. (2012). Optimal path planning of mobile robots: A review. *International Journal of the Physical Sciences*, 7:1314–1320.

Reite, K.-J., Føre, M., Aarsæther, K. G., Jensen, J., Rundtop, P., Kyllingstad, L. T., Endresen, P. C., Kristiansen, D., Johansen, V., and Fredheim, A. (2014). FhSim - time domain simulations of marine systems. In *Proc. ASME 33rd International Conference on Ocean, Offshore and Arctic Engineering*.

Rothmund, S. V., Tengesdal, T., Brekke, E. F., and Johansen, T. A. (2022). Intention modeling and inference for autonomous collision avoidance at sea. *Ocean Engineering*, 266:113080.

Rundtop, P. and Frank, K. (2016). Experimental evaluation of hydroacoustic instruments for ROV navigation along aquaculture net pens. *Aquaculture Engineering*, 74:143–156.

Sattel, T. and Brandt, T. (2008). From robotics to automotive: Lane-keeping and collision avoidance based on elastic bands. *Vehicle System Dynamics*, 46(7):597–619.

Savkin, A. V. and Wang, C. (2013). A simple biologically inspired algorithm for collision-free navigation of a unicycle-like robot in dynamic environments with moving obstacles. *Robotica*, 31(6):993–1001.

Schjølberg, I. and Utne, I. B. (2015). Towards autonomy in ROV operations. *IFAC - PapersOnLine*, 48:183–188.

Schulman, J., Duan, Y., Ho, J., Lee, A., Awwal, I., Bradlow, H., Pan, J., Patil, S., Goldberg, K., and Abbeel, P. (2014). Motion planning with sequential convex optimization and convex collision checking. *The International Journal of Robotics Research*, 33(9):1251–1270.

Shukla, A. and Karki, H. (2016). Application of robotics in offshore oil and gas industry— a review part II. *Robotics and Autonomous Systems*, 75:508–524.

Simetti, E. and Casalino, G. (2016). A novel practical technique to integrate inequality control objectives and task transitions in priority based control. *J. Intelligent & Robotic Systems*, 84(1-4):877–902.

SINTEF (2023). ACE. `https://www.sintef.no/en/all-laboratories/ace/`. Accessed: 2023-04-25.

Slagstad, D. and McClimans, T. A. (2005). Modeling the ecosystem dynamics of the barents sea including the marginal ice zone: I. Physical and chemical oceanography. *Journal of Marine Systems*, 58(1):1–18.

Slotine, J.-J. E. and Li, W. (1991). *Applied Nonlinear Control*. Prentice Hall.

Solà, J. (2017). Quaternion kinematics for the error-state Kalman filter. arXiv:1711.02508.

Su, B., Kelasidi, E., Frank, K., Haugen, J., Føre, M., and Pedersen, M. O. (2021). An integrated approach for monitoring structural deformation of aquaculture net cages. *Ocean Engineering*, 219:108424.

Su, B., Reite, K.-J., Føre, M., Aarsæther, K. G., Alver, M., Endresen, P. C., Kristiansen, D., Haugen, J., Caharija, W., and Tsarau, A. (2019). A multipurpose framework for modelling and simulation of marine aquaculture systems. In *Proc. ASME 38th International Conference on Ocean, Offshore and Arctic Engineering*.

Tengesdal, T., Rothmund, S. V., Basso, E. A., Johansen, T. A., and Schmidt-Didlaukies, H. (2023). Obstacle intention awareness in automatic collision avoidance: Full scale experiments in confined waters. *Field Robotics*. In press.

Thyri, E. H. and Breivik, M. (2022). A domain-based and reactive COLAV method with a partially COLREGs-compliant domain for ASVs operating in confined waters. *Field Robotics*, 2:637–677.

Tusseyeva, I., Kim, S.-G., and Kim, Y.-G. (2013). 3D global dynamic window approach for navigation of autonomous underwater vehicles. *International Journal of Fuzzy Logic and Intelligent Systems*, 13:91–99.

Tychonievich, L., Zaret, D., Mantegna, J., Evans, R., Muehle, E., and Martin, S. (1989). A maneuvering-board approach to path planning with moving obstacles. In *Proc. International Joint Conferences on Artificial Intelligence*, pages 1017–1021.

Wang, J., Meng, M. Q.-H., and Khatib, O. (2020). EB-RRT: Optimal motion planning for mobile robots. *IEEE Transactions on Automation Science and Engineering*, 17:2063–2073.

Wang, L., Ames, A. D., and Egerstedt, M. (2017). Safe certificate-based maneuvers for teams of quadrotors using differential flatness. In *Proc. IEEE International Conference on Robotics and Automation (ICRA)*, pages 3293–3298.

Wiig, M., Pettersen, K., and Krogstad, T. (2020). A 3D reactive collision avoidance algorithm for underactuated underwater vehicles. *J. Field Robotics*, 37:1094–1122.

Xanthidis, M., Kelasidi, E., and Alexis, K. (2023). ResiPlan: Closing the planning-acting loop for safe underwater navigation. In *Proc. IEEE International Conference on Robotics and Automation*.

Yu, L., Yang, E., Ren, P., Luo, C., Dobie, G., Gu, D., and Yan, X. (2019). Inspection robots in oil and gas industry: a review of current solutions and future trends. In *Proc. 25th International Conference on Automation and Computing (ICAC)*, pages 1–6.